Monthly Notices of the ROYAL ASTRONOMICAL SOCIETY

MNRAS **529,** 3712–3728 (2024) https://doi.org/10.1093/mnras/stae766
Advance Access publication 2024 March 15

The minimum mass for star formation by dynamical fragmentation: dependence on epoch, dust abundance, and environment

A. P. Whitworth,[1]★ F. D. Priestley,[1] R. Wünsch[2] and J. Palouš[2]

[1]*CHART, School of Physics and Astronomy, Cardiff University, Cardiff CF24 3AA, UK*
[2]*Astronomical Institute of the Czech Academy of Sciences, Boční II 1401, CZ-141 31 Prague, Czech Republic*

Accepted 2024 February 27. Received 2024 February 2; in original form 2023 June 7

ABSTRACT

We estimate the minimum mass of a star formed by dynamical collapse and fragmentation, as a function of epoch, dust abundance, and environment. Epoch is parametrized by redshift, $z_{\rm red}$, through the variation in the temperature of the cosmic microwave background. The dust abundance is parametrized by the mass-fraction in dust, $Z_{\rm D}$, with the additional simplifying assumption that the intrinsic properties of dust do not change with $Z_{\rm D}$, only the amount of dust. Environment is parametrized by the energy-density of the ambient suprathermal radiation fields through a dilution factor $\omega_\star$ (applied to a blackbody radiation field at $T_\star = 10^4$ K). The critical condition is that a spherical proto-fragment should be able to cool, and therefore contract, fast enough to detach from neighbouring proto-fragments. The minimum mass increases with increasing redshift, increasing dust abundance, and increasing suprathermal background. Values in the range from $M_{\rm MIN} \sim 0.002\,{\rm M}_\odot$ to $M_{\rm MIN} \sim 0.2\,{\rm M}_\odot$ are obtained at the extremes of the parameter ranges we have considered ($0 \leq z_{\rm red} \leq 8$, $0.00016 < Z_{\rm D} < 0.04$, and $10^{-15} \leq \omega_\star \leq 10^{-8}$). Our results agree quite well with the predictions of detailed numerical simulations invoking similar redshifts and dust abundances, but our estimates are somewhat lower; we attribute this difference to resolution issues and the small-number statistics from the simulations. The increased minimum masses predicted at high redshift and/or high suprathermal background result in significantly bottom-light initial mass functions, and therefore low mass-to-light ratios, provided that the dust abundance is not too low. The changes due to high suprathermal background may be particularly important for star formation in galactic nuclei and at high redshift.

Key words: stars: formation.

1 INTRODUCTION

This paper is concerned with estimating the minimum mass for star formation, at very low computational cost. In this context we define any self-gravitating object that forms on a dynamical time-scale, with an approximately uniform elemental composition similar to the composition of the ambient interstellar medium, as 'a star'; we therefore include as stars objects that by virtue of their mass do not ignite hydrogen (i.e. Brown Dwarfs and Planetary-Mass Objects), provided that they conform to this definition. If they do not, they are 'planets'. Basically this means that stars form more rapidly than planets, sufficiently fast that there is not enough time for significant elemental fractionation.

It seems likely that most low-mass stars form *either* by dynamical collapse and fragmentation of dense pre-stellar cores, *or* by prompt fragmentation of the accretion discs that subsequently form around the resulting first-born proto-stars (e.g. Hoyle 1953; Smith & Wright 1975; Low & Lynden-Bell 1976; Rees 1976; Silk 1977; Smith 1977; Boss 1988; Masunaga & Inutsuka 1999; Bate 2005; Boyd & Whitworth 2005; Whitworth & Stamatellos 2006; Whitworth et al. 2007; Stamatellos & Whitworth 2009; Forgan & Rice 2013; Lomax, Whitworth & Hubber 2016; Whitworth & Lomax 2016; Whitworth 2018).

Here we focus on dynamical collapse and fragmentation of dense pre-stellar cores, on the assumption (i) that the material involved in dynamical fragmentation has uniform and constant chemical composition (in particular, in a given proto-fragment the ratio of dust to gas is the same everywhere, and the properties of the dust are unchanging); and (ii) that the assembly of a proto-fragment involves transsonic or supersonic motions. We have in mind 'one-shot' fragmentation (e.g. Boyd & Whitworth 2005; Whitworth & Stamatellos 2006), rather than 'hierarchical' fragmentation (e.g. Hoyle 1953). In other words, the first fragments formed during the dynamical collapse of a pre-stellar core are unlikely to fragment again during their subsequent dynamical condensation.

Some of these assumptions cannot necessarily be made for disc fragmentation. Even if the disc material does not experience significant elemental or chemical fractionation (for example, the settling of dust to the disc mid-plane, and the growth of dust into larger entities), the initial assembly of proto-fragments in a disc may involve sub-sonic motions. Moreover, fragment growth in a disc is inevitably regulated by centrifugal acceleration – to an extent that dynamical fragmentation is not. Our conclusions may therefore not be applicable to stars formed by disc fragmentation.

★ E-mail: anthony.whitworth@astro.cf.ac.uk

Both these mechanisms (dynamical collapse and fragmentation of dense pre-stellar cores, and prompt fragmentation of protostellar accretion discs) involve low-mass proto-fragments forming in close proximity to other proto-fragments. However, there is evidence for free-floating objects with masses as low as $\sim 0.005\,\mathrm{M}_\odot$ in Upper Scorpius (Lodieu et al. 2013; Lodieu, Hambly & Cross 2021), and even lower, $\sim 0.0006\,\mathrm{M}_\odot$, in Orion (Pearson & McCaughrean 2023). There is a variety of alternative mechanisms that might form such objects. One possibility is the collapse of a very low-mass core to form a single proto-star (Machida, Inutsuka & Matsumoto 2009), but this would seem to require an unrealistically focussed and powerful ram-pressure converging from all sides to render the core unstable against contraction in the first place (e.g. Whitworth 1981; Lomax et al. 2016). Another possibility is the dynamical ejection of a newly formed protostellar embryo before it can accrete additional mass (Reipurth & Clarke 2001). Finally the photoerosion of cores overrun by H II regions (Whitworth & Zinnecker 2004) can deliver isolated low-mass stars, but only in regions that also produce the high-mass stars that ionize H II regions. The analysis we present here does not apply to these mechanisms, and in principle they offer viable pathways to form extremely low-mass stars.

In Section 2 we develop a simple one-zone model for a proto-fragment, and derive an equation of motion for its radial excursions. In Section 3 we define the conditions regulating the minimum mass, and in Section 4 we present estimates of the minimum mass as a function of the three parameters: redshift, dust abundance, and suprathermal background. In Section 5 we discuss the results, and compare them with numerical simulations and observations. Our main conclusions are summarized in Section 6. There are appendices dealing with the Planck- and Rosseland-mean opacities (A), the expressions used to represent exchange of radiant energy between a proto-fragment and its surroundings (B), the thermalization of gas and dust (C), how the results are changed if the fiducial assumptions are relaxed (D, E), and the effect on the initial mass function (IMF) (F).

2 ONE-ZONE MODEL

There are three independent variables that influence the simple one-zone model for a proto-fragment which we develop here. These are the redshift, $z_{\rm red}$, the dust abundance, $Z_{\rm D}$, and the suprathermal-background dilution factor, $\omega_\star$. We use the dust abundance, $Z_{\rm D}$, rather than the metallicity, $Z_{\rm met}$, because it appears that the relationship between the two is not simple (i.e. not linear), and $Z_{\rm D}$ is by far the more important quantity for determining the minimum mass. The relatively small influence of $Z_{\rm met}$ is discussed in Section 2.1 and evaluated in Appendix D.

We model a proto-fragment as a uniform-density sphere of radius R and mass $M_{\rm O}$. Here and in the sequel, the subscript 'O' indicates that a parameter is constant. Constant $M_{\rm O}$ means that, during the stages with which we are concerned, we neglect ongoing accretion on to a proto-fragment. It does not mean that we do not consider different values for $M_{\rm O}$.

The temperature in the sphere, T, should be viewed as a mass-weighted mean temperature.[1] T represents both the gas-kinetic temperature and the dust-vibrational temperature, since, under the circumstances with which we are concerned here, the two are very close. In other words, there is very rapid exchange of thermal energy between the gas and the dust, and the fractional difference between the gas and dust temperatures, $\Delta = [T - T_{\rm D}]/T$, is always very small ($\lesssim$0.002). We justify this assertion quantitatively in Appendix C, and values of Δ are plotted on Figs 2f, 4f, and 6f.

2.1 The mean gas-particle mass

We do not model changes in the chemical composition (dissociation, ionization, molecule formation, grain growth, and sublimation, etc.), since these processes are not expected to be significant during the brief dynamical stages with which we are concerned. Thus the mean gas-particle mass, $\bar{m}_{\rm O}$, is constant – in the sense that we do not allow it to change during the evolution of a given proto-fragment. We do however consider different values of $\bar{m}_{\rm O}$ for star formation at different dust abundances (since these will correspond to different metallicities and different helium abundances). To compute the mean gas-particle mass, $\bar{m}_{\rm O}$, we make three simplifying assumptions.

First, we assume that the elemental abundances (by mass) of hydrogen, X, helium, Y, and all other elements, $Z_{\rm met}$, are related by $X = 0.80 - 5Z_{\rm met}$ and $Y = 0.20 + 4Z_{\rm met}$. In other words, we assume that the masses of helium and 'other elements' created by stellar nucleosynthesis and delivered to the interstellar medium are at all stages in the proportion helium:other $= 4{:}1$. 'Other elements' (elements other than hydrogen and helium) are lumped together, labelled 'metals', and represented collectively by 'oxygen'.

Secondly, we assume that all the hydrogen and 'oxygen' are molecular (for simplicity, respectively H_2 and O_2). The mean gas-particle mass is then given by

$$\bar{m}_{\rm O}(Z_{\rm met}) = \frac{m_{\rm H}}{X/2 + Y/4 + Z_{\rm met}/32} = \frac{32\,m_{\rm H}}{14.4 - 47Z_{\rm met}}, \qquad (1)$$

where $m_{\rm H}$ is the mass of an hydrogen atom. To the level of accuracy with which we are concerned, the results are not changed if we take into account heavy molecules other than O_2, e.g. CO.

Thirdly, we need to consider how the metallicity, $Z_{\rm met}$, varies with the dust abundance, $Z_{\rm D}$ (e.g. De Vis et al. 2019; Galliano et al. 2021; Konstantopoulou et al. 2024). As we note below, fractional changes in $\bar{m}_{\rm O}$ are small. Therefore, we adopt a very approximate fit to the results in Galliano et al. (2021; their fig. 12b),

$$Z_{\rm D} = \frac{Z_{\rm met}^2}{2\,[Z_{\rm met} + 0.007]}, \qquad (2)$$

from which we obtain

$$Z_{\rm met} = Z_{\rm D}\left\{1 + \left[1 + \frac{0.014}{Z_{\rm D}}\right]^{1/2}\right\}. \qquad (3)$$

With this fit, $Z_{\rm met}$ and $\bar{m}_{\rm O}$ increase from $[Z_{\rm met}, \bar{m}_{\rm O}] = [0.0016,\ 3.74\times10^{-24}\,\mathrm{g}]$ when $Z_{\rm D} = 0.00016$, to $[Z_{\rm met}, \bar{m}_{\rm O}] = [0.0255,\ 4.06\times10^{-24}\,\mathrm{g}]$ when $Z_{\rm D} = 0.01$ (i.e. this 64-fold increase in dust abundance only produces an 8 per cent increase in $\bar{m}_{\rm O}$). For higher dust abundances the increases are somewhat more significant: when $Z_{\rm D} = 0.04$, $[Z_{\rm met}, \bar{m}_{\rm O}] = 0.086,\ 5.17\times10^{-24}\,\mathrm{g}]$ (i.e. the fourfold increase in $Z_{\rm D}$ from 0.01 to 0.04 produces a 27 per cent increase in $\bar{m}_{\rm O}$).

In Appendix D we explore how the results are changed if we replace equation (3) with the simpler linear relation $Z_{\rm met} = 2Z_{\rm D}$ (i.e.

[1] In general there will be an inward temperature gradient ($\mathrm{d}T/\mathrm{d}r < 0$) throughout most of the interior of the proto-fragment. This gradient is usually quite small (in the sense that $T_{\rm CENTRE} \lesssim 1.3T_{\rm EDGE}$), and never very large (in the sense that $T_{\rm CENTRE} \lesssim 5T_{\rm EDGE}$). This is because the optical depth through a proto-fragment is normally $\lesssim$1 and always $\lesssim$1000 (see Section 5.1 and Figs 2b, 4b, and 6b)

under all circumstances, half the metals are in dust and half in the gas-phase). Provided the results are presented as a function of $Z_{\rm D}$ (and not $Z_{\rm met}$), there is little change. At low $Z_{\rm D}$, with high $z_{\rm red}$ and/or high $\omega_\star$, $M_{\rm MIN}$ is slightly reduced.

Reality is of course more complicated, since different elements are produced by stars with different masses and different evolutionary time-scales. Moreover, stars of different mass may be formed in different proportions at different epochs and in different environments. Consequently the accumulation of different elements in the interstellar medium and their incorporation into dust proceed on different schedules (e.g. Goswami et al. 2022; Sharda et al. 2023). However, consideration of such refinements is not justified here, given the uncertainties in other aspects of the physics. Equations (1) and (3) probably capture adequately the dependence of $\bar{m}_{\rm O}$ on $Z_{\rm D}$, in the sense that $\bar{m}_{\rm O}$ tends to increase monotonically but not linearly with increasing $Z_{\rm D}$.

2.2 The energy equation

We assume that the temperature in a proto-fragment is regulated by an energy equation of the form

$$\begin{aligned}\frac{{\rm d}U}{{\rm d}t} &= \frac{3M_{\rm O}k_{\rm B}}{2\bar{m}_{\rm O}}\,\frac{{\rm d}T}{{\rm d}t}\\ &= -\,\frac{3M_{\rm O}k_{\rm B}T}{\bar{m}_{\rm O}R}\,\frac{{\rm d}R}{{\rm d}t} + \frac{4\pi R^2\sigma_{\rm SB}T_{\rm CMB}^4}{\bar{\tau}_{\rm RO}(T_{\rm CMB})+\bar{\tau}_{\rm PL}^{-1}(T_{\rm CMB})}\\ &\quad + \Gamma_\star(\omega_\star, M_{\rm O}, R) - \frac{4\pi R^2\sigma_{\rm SB}T^4}{\bar{\tau}_{\rm RO}(T)+\bar{\tau}_{\rm PL}^{-1}(T)}.\end{aligned} \tag{4}$$

Here $U = 3M_{\rm O}k_{\rm B}T/2\bar{m}_{\rm O}$ is the total thermal energy of the proto-fragment, $k_{\rm B}$ is the Boltzmann constant, and $\sigma_{\rm SB}$ is the Stefan–Boltzmann constant. We are assuming that the temperature is always low (i.e. usually $T \lesssim 50\,{\rm K}$ and always $T \lesssim 200\,{\rm K}$), so that for the common gas species (H_2 and He) only the translational degrees of freedom are significantly excited. This is justified retrospectively in Section 5.1 (also see Figs 2a, 4a, and 6a).

On the right-hand side of equation (4), the first term is the compressional heating rate, and the remaining three terms represent exchange of radiation with the surroundings. These three terms are formulated in the order: (i) absorption of cosmic microwave background (CMB) radiation, (ii) absorption of ambient suprathermal radiation, and (iii) thermal emission from dust.

The temperature of the CMB in equation (4) is given by

$$T_{\rm CMB} = 2.73\,{\rm K}\,[1+z_{\rm red}], \tag{5}$$

where $z_{\rm red}$ is the redshift. This is the only dependence on $z_{\rm red}$ that we include explicitly, and represents changing epoch. In the denominator (below $T_{\rm CMB}^4$ in equation 4), $\bar{\tau}_{\rm RO}(T_{\rm CMB})$ and $\bar{\tau}_{\rm PL}(T_{\rm CMB})$ are, respectively, the Rosseland- and Planck-mean optical depths presented to the CMB radiation by the dust in the proto-fragment. For the redshifts with which we are concerned, the cosmic background radiation remains predominantly in the microwave region of the electromagnetic spectrum. The CMB heating term is analysed further in Appendix B3.

The local suprathermal background is represented by a blackbody spectrum at a fixed notional temperature, $T_\star = 10^4\,{\rm K}$ (approximately the surface temperature of an A0 star), but diluted by a factor $\omega_\star$ (see Spitzer 1978, his equation 4-13 and the associated text). Hence there is a flux

$$F_\star = \omega_\star\,\sigma_{\rm SB}\,T_\star^4 \tag{6}$$

incident on the boundary of the star-forming molecular cloud. In the general interstellar medium in the solar vicinity, $\omega_\star \sim 10^{-14}$, but in other locations $\omega_\star$ may be significantly larger. Thus $\omega_\star$ is the parameter representing different environments.

However, suprathermal radiation will not penetrate very far into a proto-fragment, because the dust optical depth presented to suprathermal radiation at $\sim 0.3\,\mu{\rm m}$ is very large. Indeed, the boundary of the proto-fragment may be shielded from direct suprathermal irradiation by more widely distributed dust in the outskirts of its parent molecular cloud. Consequently, by the time this radiation reaches the deep interior of the proto-fragment, it has been degraded to much longer wavelengths by repeated absorption and re-emission. There is no simple expression for this process. In Appendix B4 we formulate an approximate procedure to track the penetration of incident suprathermal radiation into the interior of a proto-fragment, and thereby estimate the associated heating rate.

There could also be a term representing heating by incident cosmic-rays, but we shall assume that an increase in the flux of cosmic-rays incident on the boundary of a proto-fragment is likely to be accompanied by an increase in the flux of suprathermal radiation incident on the boundary of the proto-fragment. Therefore, in the interests of keeping the parameter-space small, it can be accommodated within $\omega_\star$. Moreover, the role of cosmic rays in heating a proto-fragment is probably small, as inferred observationally by Yang et al. (2023), and argued theoretically by Low & Lynden-Bell (1976).

The final term on the right-hand side of equation (4) represents thermal emission from dust in the proto-fragment. In the denominator (below T^4 in equation 4), $\bar{\tau}_{\rm RO}(T)$ and $\bar{\tau}_{\rm PL}(T)$ are, respectively, the Rosseland- and Planck-mean optical depths presented by the dust in the proto-fragment to its own emission. The dust cooling term is analysed in Appendices B1 and B2.

2.3 Dust and optical depths

If all dust grains are spherical, the net geometric cross-section presented by unit mass of dust is

$$\kappa_{\rm O} = \frac{3}{4}\left\langle\frac{1}{r_{\rm D}\rho_{\rm D}}\right\rangle_{\rm mass\ weighted}. \tag{7}$$

Here $r_{\rm D}$ is the radius of a dust grain, $\rho_{\rm D}$ is the internal density of a dust grain, and the average in equation (7) is mass weighted. We adopt the value

$$\kappa_{\rm O} \simeq 2\times10^4\,{\rm cm^2\,g^{-1}}. \tag{8}$$

The monochromatic opacity of the dust κ_λ (i.e. the cross-section presented by unit mass of dust to radiation with wavelength λ) is taken from Mathis (1990), and converted into Planck- and Rosseland-mean opacities, $\bar{\kappa}_{\rm PL}(T)$ and $\bar{\kappa}_{\rm RO}(T)$, as described in Appendix A. For simplicity we assume that $\kappa_{\rm O}$, κ_λ, $\bar{\kappa}_{\rm PL}(T)$, and $\bar{\kappa}_{\rm RO}(T)$ are invariant. In other words the mix of different grain types is the same everywhere and at all epochs, and only the abundance of dust, $Z_{\rm D}$, changes. In reality there are likely to be variations, due both to the different circumstances under which dust nucleation and growth can occur, and differences in the local elemental and chemical abundances (e.g. Clark et al. 2023; Hu, Sternberg & van Dishoeck 2023).

The column-density between the centre of a proto-fragment and its surface is

$$\Sigma = \frac{3M_{\rm O}}{4\pi R^2}. \tag{9}$$

The Rosseland- and Planck-mean optical depths – which control the penetration of externally incident CMB and suprathermal radiation, and the escape of internally emitted radiation from dust – are then given by

$$\bar{\tau}_{\rm RO}(T') = \Sigma\, Z_{\rm D}\, \bar{\kappa}_{\rm RO}(T'), \tag{10}$$

$$\bar{\tau}_{\rm PL}(T') = \Sigma\, Z_{\rm D}\, \bar{\kappa}_{\rm PL}(T'), \tag{11}$$

where T' is the temperature of the radiation under consideration.

2.4 The equation of radial motion

Radial excursions of the proto-fragment are regulated by an equation of motion, which in the absence of significant external pressure takes the form

$$\frac{{\rm d}^2 R}{{\rm d}t^2} = -\frac{G M_{\rm O}}{R^2} + \frac{5 k_{\rm B} T}{\bar{m}_{\rm O} R}. \tag{12}$$

In equation (12), the first term on the right-hand side represents the inward acceleration due to self-gravity, and the second term represents the outward acceleration due to internal thermal pressure. It follows that the condition for gravitational contraction (i.e. the Jeans criterion) is

$$R < R_{\rm JEANS} = \frac{G M_{\rm O} \bar{m}_{\rm O}}{5 k_{\rm B} T}. \tag{13}$$

3 THE MINIMUM MASS

A proto-fragment will only condense out if it satisfies three conditions. Condition 1: it must be gravitationally unstable (i.e. it must obey Inequality 13). Condition 2: it must contract fast enough to condense out independently, i.e. to separate from neighbouring fragments. Condition 3: it must stay cool, so that it continues to separate from its surroundings.

There is latitude in formulating Condition 2. Some authors (e.g. Rees 1976) posit that the boundary of the proto-fragment must contract faster than the sonic speed,

$$-\frac{{\rm d}R}{{\rm d}t} \geq -\frac{{\rm d}R}{{\rm d}t}_{\rm SONIC} = \left[\frac{k_{\rm B} T}{\bar{m}_{\rm O}}\right]^{1/2}, \tag{14}$$

in order to detach from its surroundings; this choice is probably appropriate if the surroundings are stationary. Other authors posit that the boundary of the proto-fragment must contract faster than the freefall speed,

$$-\frac{{\rm d}R}{{\rm d}t} \geq -\frac{{\rm d}R}{{\rm d}t}_{\rm FREEFALL} = \left[\frac{2\,G\,M_{\rm O}}{R}\right]^{1/2}, \tag{15}$$

in order to detach from its surroundings; this choice is probably appropriate if the surroundings represent a larger cloud that is itself also approaching freefall collapse.

In the sequel we adopt the sonic case. However, for a marginally Jeans unstable proto-fragment (which is the circumstance on which we need to focus to estimate the minimum mass),

$$\frac{{\rm d}R}{{\rm d}t}_{\rm FREEFALL} = -\left[\frac{10 k_{\rm B} T}{\bar{m}_{\rm O}}\right]^{1/2} = 10^{1/2}\,\frac{{\rm d}R}{{\rm d}t}_{\rm SONIC}. \tag{16}$$

Therefore, in the analysis presented below, the freefall case can be invoked simply by replacing $f_{\rm SONIC} = 1$ with $f_{\rm FREEFALL} = 10^{1/2}$ in equation (17). In Appendix E we evaluate by how much the minimum mass is increased if the freefall case is adopted in place of the sonic case.

To estimate the minimum mass, we consider a proto-fragment that only just satisfies Conditions 1 through 3. Condition 1 is marginally satisfied if $R = R_{\rm JEANS}$ (see equation 13). Condition 2 is marginally satisfied if ${\rm d}R/{\rm d}t = {\rm d}R/{\rm d}t_{\rm SONIC} = f_{\rm SONIC}[k_{\rm B}T/\bar{m}_{\rm O}]^{1/2}$ for the sonic case, or ${\rm d}R/{\rm d}t = {\rm d}R/{\rm d}t_{\rm FREEFALL} = f_{\rm FREEFALL}[k_{\rm B}T/\bar{m}_{\rm O}]^{1/2}$ for the freefall case (see equation 16 and postscript). Condition 3 is marginally satisfied if ${\rm d}U/{\rm d}t = 0$ (see equation 4). Combining these conditions, we obtain

$$\frac{f_{\rm SONIC} 3^2 5^4 m_{\rm PL}^6}{\pi^3 M_{\rm O}^2 \bar{m}_{\rm O}^4}\left[\frac{k_{\rm B}T}{\bar{m}_{\rm O}c^2}\right]^{1/2} T^4 + \frac{T_{\rm CMB}^4}{\bar{\tau}_{\rm RO}(T_{\rm CMB}) + \bar{\tau}_{\rm PL}^{-1}(T_{\rm CMB})} + \frac{\Gamma_\star}{4\pi R^2 \sigma_{\rm SB}} - \frac{T^4}{\bar{\tau}_{\rm RO}(T) + \bar{\tau}_{\rm PL}^{-1}(T)} = 0. \tag{17}$$

The four terms in equation (17) represent, in sequence, compressional heating, heating by the CMB, heating by the suprathermal background radiation field, and cooling by thermal dust emission; $m_{\rm PL} = [hc/2\pi G]^{1/2} = 2.18 \times 10^{-5}$ g is the Planck mass.

The column-density (equation 9) – and hence the optical depths in equation (17) (see equations 10 and 11) – must be computed with $R = R_{\rm JEANS}$, hence

$$\Sigma = \frac{75}{4\pi G^2 M_{\rm O}}\left[\frac{k_{\rm B}T}{\bar{m}_{\rm O}}\right]^2. \tag{18}$$

4 RESULTS

In order to solve equation (17), we must specify (i) the redshift, $z_{\rm red}$, since this determines $T_{\rm CMB}$ (equation 5); (ii) the dust abundance, $Z_{\rm D}$, since this determines the dust opacities, $\bar{\tau}_{\rm RO}(T)$ and $\bar{\tau}_{\rm PL}(T)$ (see equations 10 and 11) and also the mean gas-particle mass, $\bar{m}_{\rm O}$ (equation 1); and (iii) the suprathermal background parameter, $\omega_\star$, which determines the strength of the ambient suprathermal radiation field (equation 6).

We have solved equation (17) numerically for all 62 073 combinations of (i) $z_{\rm red} = 0.00, 0.25, 0.50, \cdots, 7.75, 8.00$ (33 values equally spaced arithmetically by 0.25); (ii) $Z_{\rm D} = 0.00015625, 0.00018581, 0.00022097, \cdots, 0.03363582, 0.04000000$ (33 values equally spaced geometrically by a factor $2^{1/4}$); and (iii) $\log_{10}(w_\star) = -15.000, -14.875, -14.750, \cdots, -8.125, -8.000$ (57 values equally spaced arithmetically by 0.125).

We adopt as fiducial values $z_{\rm red} = 0$ (now), $Z_{\rm D} = 0.01$ (approximately the current dust abundance in the interstellar medium in the Solar vicinity), and $\omega_\star = 10^{-14}$ (approximately the current suprathermal radiation field in the Solar vicinity).

The method of solution for a given parameter set, ($z_{\rm red}$, $Z_{\rm D}$, $\omega_\star$), involves finding the solution of equation (17) in the form $M_{\rm O}(T)$, and then identifying the smallest $M_{\rm O}(T)$ as $M_{\rm MIN}(z_{\rm red}, Z_{\rm D}, \omega_\star)$. This also gives the temperature, $T_{\rm CRIT}$, dust optical depth, $\bar{\tau}_{\rm CRIT}$, radius, $R_{\rm CRIT}$, density, $\rho_{\rm CRIT}$, pressure, $P_{\rm CRIT}$, and fractional difference between the gas and dust temperatures, $\Delta_{\rm CRIT} = (T - T_{\rm D})/T$ in the minimum mass proto-fragment, at its inception (see Appendix C).

For $\bar{\tau}_{\rm CRIT}$ we use an effective optical depth,

$$\bar{\tau}_{\rm CRIT} = \frac{\bar{\tau}_{\rm RO}^2(T_{\rm CRIT}) + 1}{\bar{\tau}_{\rm RO}(T_{\rm CRIT}) + \bar{\tau}_{\rm PL}^{-1}(T_{\rm CRIT})}. \tag{19}$$

This gives $\sim \bar{\tau}_{\rm RO}(T_{\rm CRIT})$ in the optically thick limit (i.e. where $\bar{\tau}_{\rm RO}$ is the functioning optical depth, $\bar{\tau}_{\rm RO}(T_{\rm CRIT}) \gg 1$); $\sim \bar{\tau}_{\rm PL}(T_{\rm CRIT})$ in the optically thin limit (i.e. where $\bar{\tau}_{\rm PL}$ is the functioning optical depth, $\bar{\tau}_{\rm PL}(T_{\rm CRIT}) \ll 1$); and ~ 1 where the optical depth is of order unity, i.e. $\bar{\tau}_{\rm RO}(T_{\rm CRIT}) \sim \bar{\tau}_{\rm PL}(T_{\rm CRIT}) \sim 1$.

For the purpose of labelling figures, we use (i) the value of $z_{\rm red}$, specifically the values $z_{\rm red} = 0$, 2, 4, 6, and 8; (ii) the value of

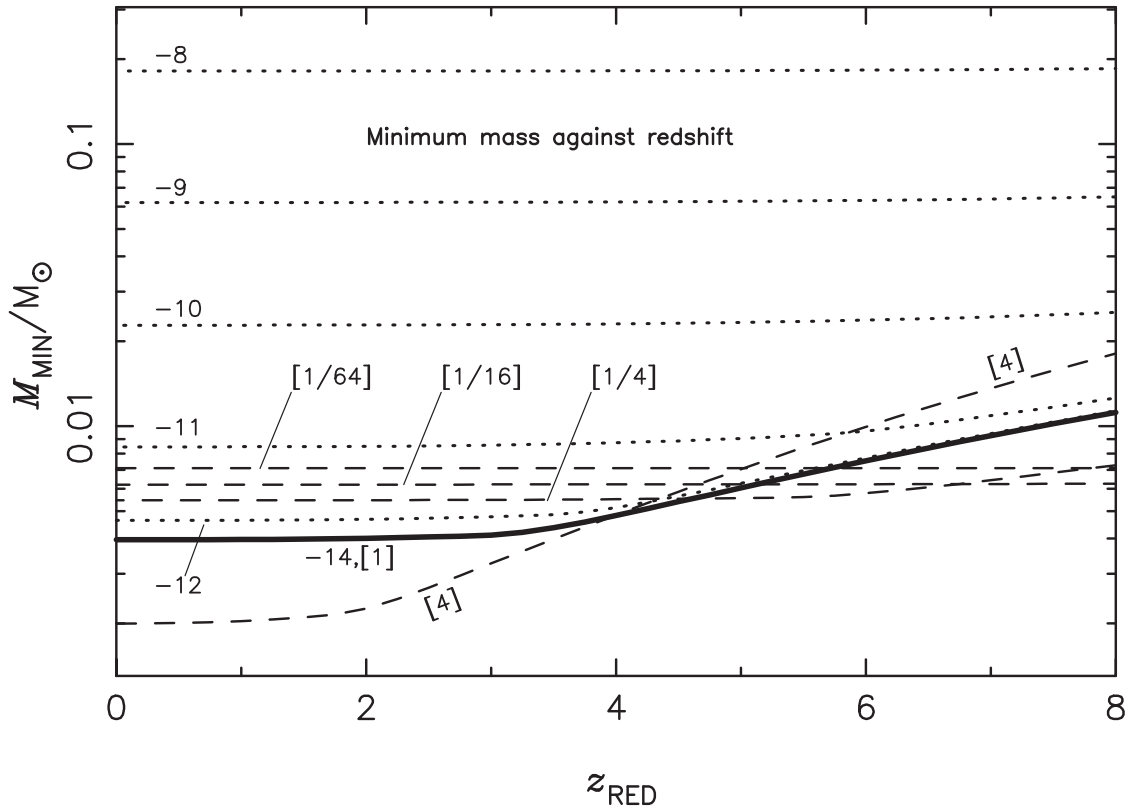

Figure 1. The variation of the minimum mass, $M_{\rm MIN}$, with the redshift, $z_{\rm red}$. The full curve labelled '−14, [1]' shows $M_{\rm MIN}(z_{\rm red})$ for models with the fiducial values of suprathermal background, $\log_{10}(\omega_\star) = -14$, and dust abundance, $[Z_{\rm D}/0.01] = [1]$. The dashed curves show $M_{\rm MIN}(z_{\rm red})$ for models with, from top to bottom, different dust abundances, $[Z_{\rm D}/0.01] = [1/64]$, [1/16], [1/4], and [4], but the same fiducial suprathermal background as the full curve, i.e. $\log_{10}(\omega_\star) = -14$. The dotted curves show $M_{\rm MIN}(z_{\rm red})$ for models with, from bottom to top, different suprathermal backgrounds, $\log_{10}(\omega_\star) = -12$, −11, −10, −9, and −8, but the same fiducial dust abundance as the full curve, i.e. $[Z_{\rm D}/0.01] = [1]$. The ordinate is scaled logarithmically. The same line-styles and labelling system are used on Fig. 2, which shows the corresponding variations of $T_{\rm CRIT}$, $\bar{\tau}_{\rm CRIT}$, $R_{\rm CRIT}$, $\rho_{\rm CRIT}$, $P_{\rm CRIT}$, and $\Delta_{\rm CRIT}$.

$Z_{\rm D}$, normalized to 0.01, specifically the values $[Z_{\rm D}/0.01] = [1/64]$, [1/16], [1/4], [1], and [4]; and (iii) the logarithm of the suprathermal dilution factor, $\log_{10}(w_\star)$, specifically the values $\log_{10}(w_\star) = -15$, −14, −13, −12, −11, −10, −9, and −8. The fiducial set is therefore labelled with $z_{\rm red} = 0$, $[Z_{\rm D}/0.01] = [1]$ and $\log_{10}(w_\star) = -14$, and is always plotted with a bold full curve.

4.1 Variation of the minimum mass with redshift

Fig. 1 shows the variation of the minimum mass, $M_{\rm MIN}$, with the redshift, $z_{\rm red}$. On Fig. 2, we show – using the same line-styles and labelling – the corresponding variations in (a) the temperature, $T_{\rm CRIT}$, (b) the dust-emission optical depth, $\bar{\tau}_{\rm CRIT}$, (c) the radius, $R_{\rm CRIT}$, (d) the density, $\rho_{\rm CRIT}$, (e) the pressure, $P_{\rm CRIT}$, and (f) the fractional difference between the gas and dust temperatures, $\Delta_{\rm CRIT}$, for the minimum-mass proto-fragment at its inception.

The full curves on Figs 1 and 2 show the fiducial case, i.e. $[Z_{\rm D}/0.01] = [1]$ and $\log_{10}(\omega_\star) = -14$. The minimum mass increases monotonically with increasing redshift, due to the associated increase in the microwave background temperature, but this increase only becomes significant at redshifts $z_{\rm red} \gtrsim 4$. The increase is largely due to an increase in temperature, due to the proto-fragments switching from being optically thin to being optically thick. The radius and density of a minimum-mass proto-fragment are only weakly dependent on redshift.

The dashed curves on Figs 1 and 2 show how the minimum mass varies with redshift if the suprathermal background is fixed at its fiducial value, $\log_{10}(w_\star) = -14$, but different values of the dust abundance are considered (i.e. $[Z_{\rm D}/0.01] = [1/64]$, [1/16], [1/4], and [4]); if we include the fiducial case ($[Z_{\rm D}/0.01] = [1]$), there is a geometrical sequence of five dust abundances spaced by factors of 4. For metallicities above (*vice* below) the fiducial value ($Z_{\rm D} \sim 0.01$) proto-fragments become optically thick at lower (higher) redshifts, and therefore the accompanying increases in temperature occur at lower (higher) redshifts, and the resulting increases in the minimum mass are greater and steeper (smaller and shallower), as shown on Figs 2a and 2b.

The dotted curves on Figs 1 and 2 show how the minimum mass varies with redshift if the dust abundance is held constant at its fiducial value, $Z_{\rm D} = 0.01$, but different values of the suprathermal background are considered ($\log_{10}(\omega_\star) = -12$, −11, −10, −9, and −8); thus there is a geometrical sequence of five suprathermal backgrounds spaced by factors of 10, but starting well above the fiducial value ($\log_{10}(\omega_\star) = -14$). The redshift is only an important determinant of the minimum mass if it is high enough that the energy density of the CMB exceeds that of the suprathermal background, i.e.

$$z_{\rm red} \gtrsim \frac{\omega_\star^{1/4}\, T_\star}{2.73\,{\rm K}} - 1 \simeq 3663\, \omega_\star^{1/4} - 1; \qquad (20)$$

in these cases the mass and other properties of a minimum-mass

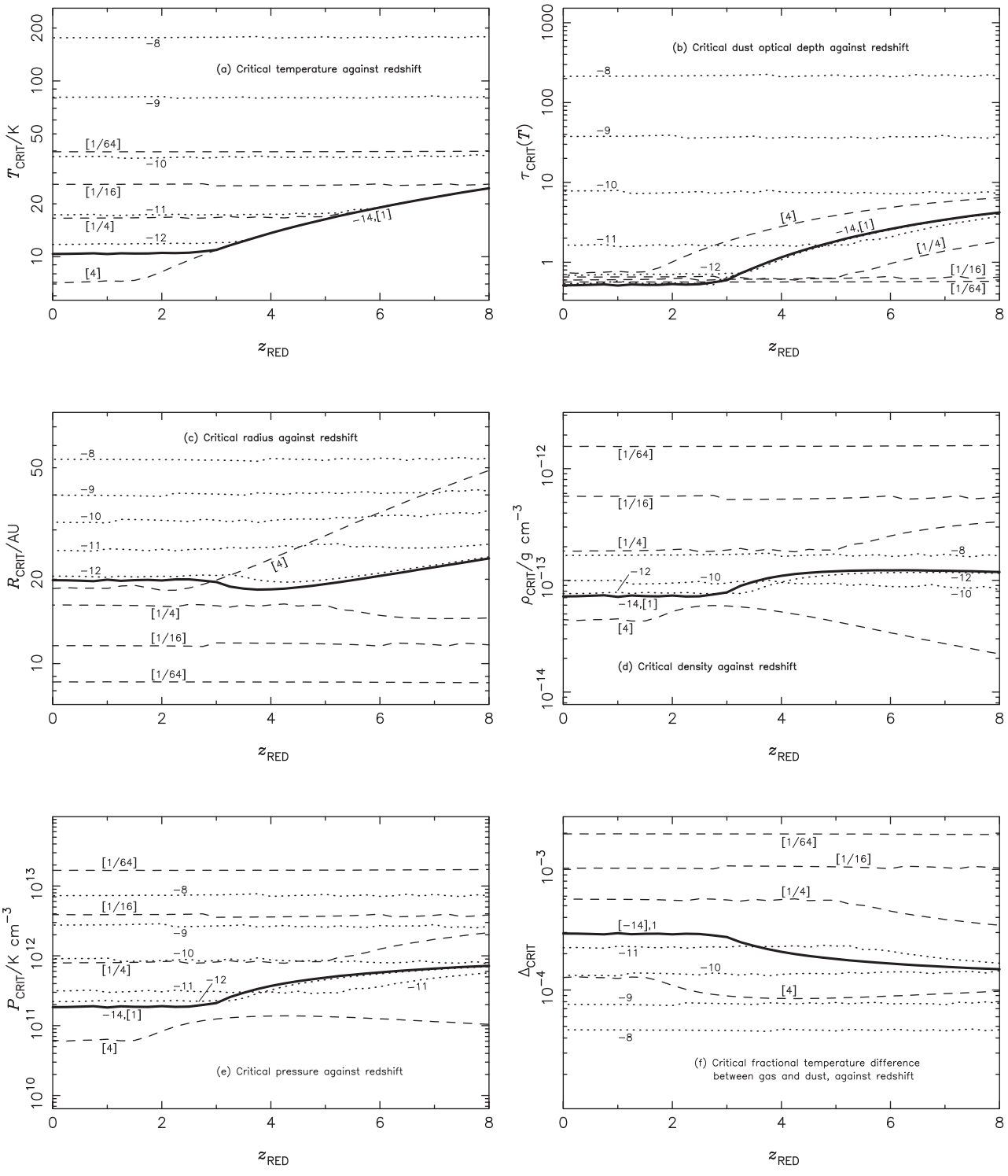

Figure 2. Plots showing the variation with redshift, $z_{\rm red}$, of (a) the critical temperature, $T_{\rm CRIT}$, (b) the critical dust-emission optical depth, $\bar{\tau}_{\rm CRIT}$, (c) the critical radius, $R_{\rm CRIT}$, (d) the critical density, $\rho_{\rm CRIT}$, (e) the critical pressure, $P_{\rm CRIT}$, and (f) the critical fractional difference between the gas and dust temperatures, $\Delta_{\rm CRIT}$, for representative combinations of the dust abundance, $Z_{\rm D}$, and the background suprathermal radiation field, $\omega_\star$. The full curve represents the fiducial combination, i.e. $[Z_{\rm D}/0.01] = [1]$ and $\log_{10}(\omega_\star) = -14$. The dashed curves show how the results change if the dust abundance is changed, i.e. $[Z_{\rm D}/0.01] =$ [1/64], [1/16], [1/4], and [4], but the suprathermal radiation field is held constant at $\log_{10}(\omega_\star) = -14$. The dotted curves show how the results change if the suprathermal radiation field is changed, i.e. $\log_{10}(\omega_\star) = -12$, -11, -10, -9, and -8, but the dust abundance is held constant at $[Z_{\rm D}/0.01] = [1]$. Curves are not drawn where they are too close to the fiducial curve to be resolved. On all plots the ordinate is scaled logarithmically.

proto-fragment then vary with redshift in a similar way to the fiducial case.

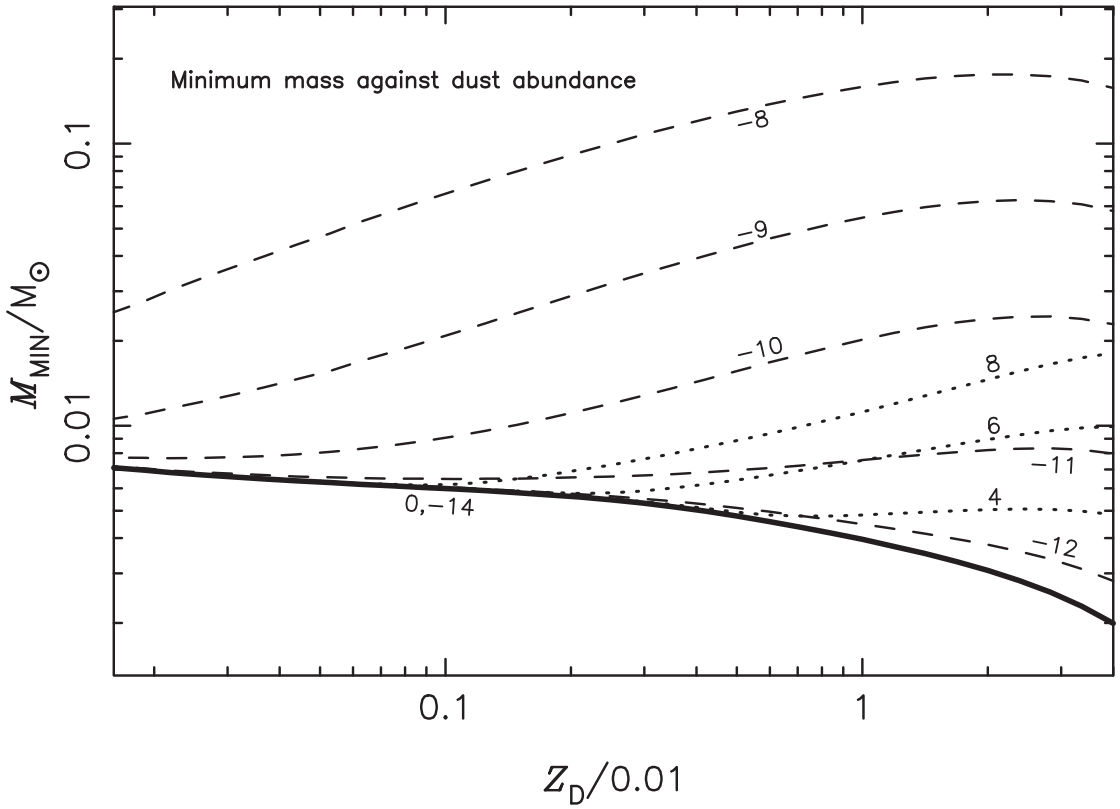

Figure 3. The variation of the minimum mass, $M_{\rm MIN}$, with the dust abundance, $Z_{\rm D}$. The full curve labelled '0,-14' shows $M_{\rm MIN}(Z_{\rm D})$ for models with the fiducial values of redshift, $z_{\rm red} = 0$, and suprathermal background, $\log_{10}(\omega_\star) = -14$. The dashed curves show $M_{\rm MIN}(Z_{\rm D})$ for models with, from bottom to top, different suprathermal backgrounds, $\log_{10}(\omega_\star) = -12$, -11, -10, -9, and -8, but the same fiducial redshift as the full curve, i.e. $z_{\rm red} = 0$. The dotted curves show $M_{\rm MIN}(Z_{\rm D})$ for models with, from bottom to top, different redshifts. $z_{\rm red} = 2$, 4, 6, and 8, but the same fiducial suprathermal background as the full curve, i.e. $\log_{10}(\omega_\star) - 14$. Both axes are scaled logarithmically. The same line-styles and labelling system are used on Fig. 4, which shows the corresponding variations of $T_{\rm CRIT}$, $\bar{\tau}_{\rm CRIT}$, $R_{\rm CRIT}$, $\rho_{\rm CRIT}$, $P_{\rm CRIT}$, and $\Delta_{\rm CRIT}$.

4.2 Variation of the minimum mass with dust abundance

Fig. 3 shows the variation of the minimum mass with the dust abundance, $Z_{\rm D}$. On Fig. 4, we show – using the same line-styles and labelling – the corresponding variations in $T_{\rm CRIT}$, $\bar{\tau}_{\rm CRIT}$, $R_{\rm CRIT}$, $\rho_{\rm CRIT}$, $P_{\rm CRIT}$, and $\Delta_{\rm CRIT}$, for the minimum-mass proto-fragment at its inception.

The full curves on Figs 3 and 4 show the fiducial case, i.e. $z_{\rm red} = 0$ and $\log_{10}(w_\star) = -14$. The minimum mass decreases monotonically with increasing dust abundance. The CMB is not significantly attenuated, even at the higher dust abundances, and the suprathermal background is too weak to heat the proto-fragment significantly. Consequently we are in the optically thin regime: increased dust abundance results in increased dust cooling (rather than trapping of cooling radiation), reduced temperature, and reduced minimum mass. The radius of the minimum mass proto-fragment increases somewhat with increasing dust abundance, until the fiducial dust abundance is reached, but this is compensated by a decrease in density.

The dashed curves on Figs 3 and 4 show how the minimum mass varies with the dust abundance if the redshift is fixed at its fiducial value, $z_{\rm red} = 0$, but different values for the suprathermal background are considered (i.e. $\log_{10}(\omega_\star) = -12, -11, -10, -9,$ and -8). If there is a strong suprathermal background ($\omega_\star \gtrsim 10^{-10}$), the minimum mass increases quite rapidly with increasing dust abundance. This is because the dust temperature is raised, and the proto-fragment becomes optically thick and extended.

The dotted curves on Figs 3 and 4 show how the minimum mass varies with the dust abundance if the suprathermal background is fixed at its fiducial value, $\log_{10}(\omega_\star) = -14$, but different values for the redshift are considered (i.e. $z_{\rm red} = 2$, 4, 6, and 8); thus, if we include the fiducial case there is an arithmetic sequence of five redshifts with a spacing of 2. At higher redshift the CMB is hotter and more intense, and therefore more effective at heating the proto-fragment. Specifically, at redshift $z_{\rm red}$, if the dust abundance is sufficiently large to trap the cooling radiation,

$$z_{\rm red} \gtrsim \left[\frac{Z_{\rm D}}{0.002}\right]^{-1}, \tag{21}$$

the minimum mass increases with increasing redshift.

4.3 Variation of the minimum mass with suprathermal background

Fig. 5 shows the variation of the minimum mass with the suprathermal background, $\omega_\star$. On Fig. 6, we show – using the same line-styles and labelling – the corresponding variations in $T_{\rm CRIT}$, $\bar{\tau}_{\rm CRIT}$, $R_{\rm CRIT}$, $\rho_{\rm CRIT}$, $P_{\rm CRIT}$, and $\Delta_{\rm CRIT}$, for the minimum-mass proto-fragment at its inception.

The full curves on Figs 5 and 6 show the fiducial case, i.e. $z_{\rm red} = 0$ and $[Z_{\rm D}/0.01] = [1]$. The minimum mass increases monotonically with increasing suprathermal background, $\omega_\star$, due to the consequent increase in the heating rate, and hence the temperature, the optical

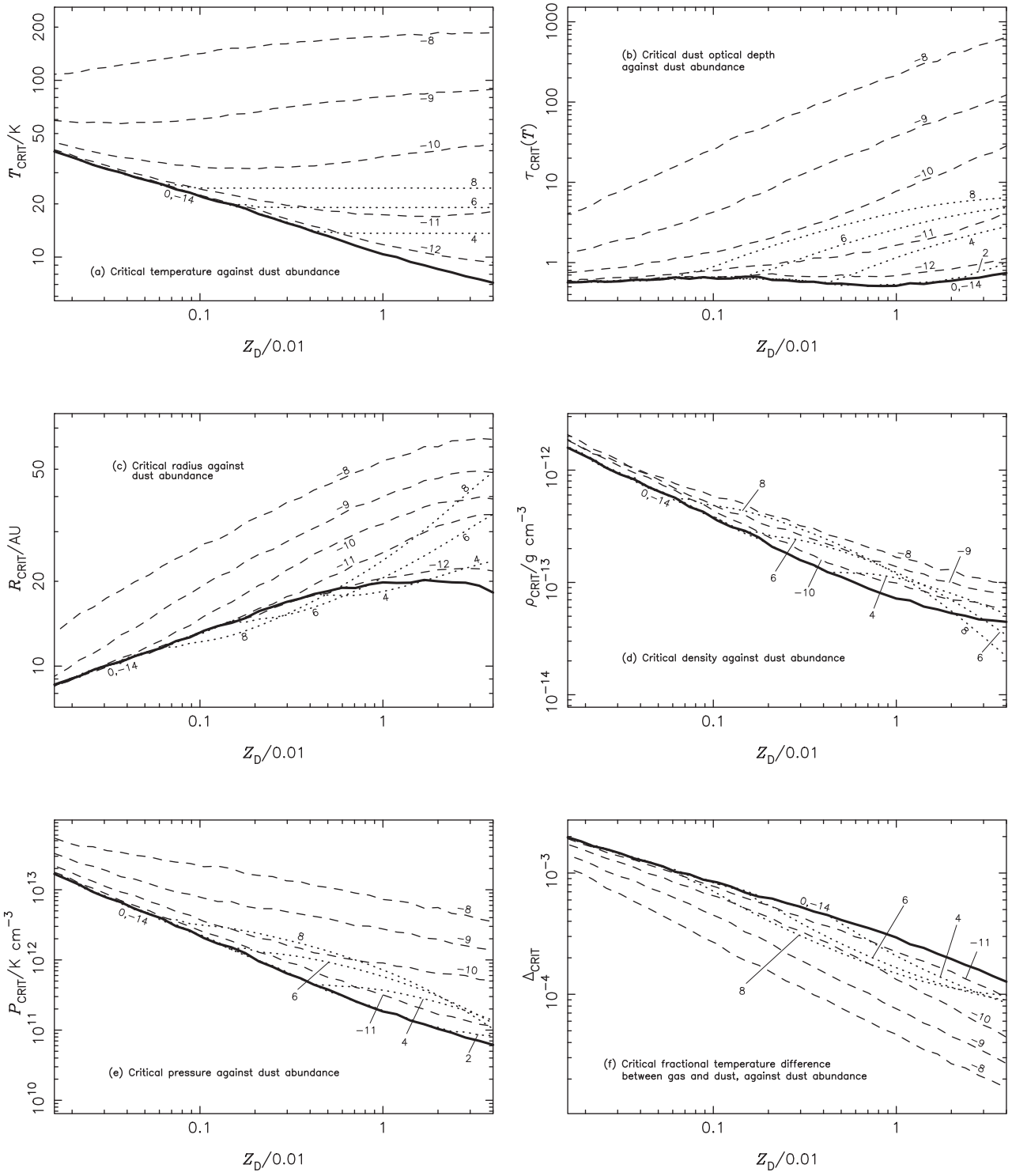

Figure 4. Plots showing the variation with dust abundance, Z_D, of (a) the critical temperature, T_{CRIT}, (b) the critical dust-emission optical depth, $\bar{\tau}_{CRIT}$, (c) the critical radius, R_{CRIT}, (d) the critical density, ρ_{CRIT}, (e) the critical pressure, P_{CRIT}, and (f) the critical fractional difference between the gas and dust temperatures, Δ_{CRIT}, for representative combinations of the background suprathermal radiation field, $\omega_\star$, and the redshift, z_{red}. The full curve represents the fiducial combination, i.e. $\log_{10}(\omega_\star) = -14$ and $z_{red} = 0$. The dashed curves show how the results change if the suprathermal background radiation field is changed, i.e. $\log_{10}(\omega_\star) = -12$, -11, -10, -9, and -8, but the redshift is held constant at $z_{red} = 0$. The dotted curves show how the results change if the redshift is changed, i.e. $z_{red} = 2$, 4, 6, and 8, but the suprathermal background radiation field is held constant at $\omega_\star = -14$. On all plots both axes are scaled logarithmically.

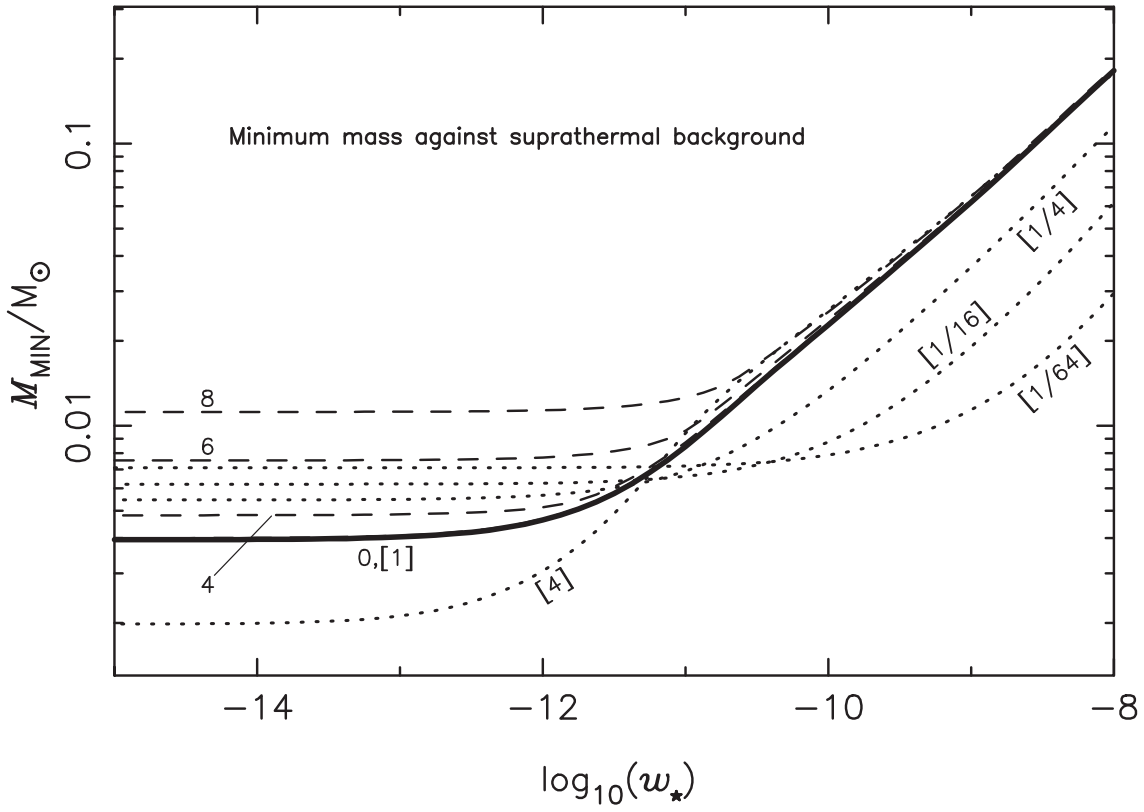

Figure 5. The variation of the minimum mass, $M_{\rm MIN}$, with the suprathermal background, $\omega_\star$. The full curve shows $M_{\rm MIN}(\omega_\star)$ for models with the fiducial values of redshift, $z_{\rm red} = 0$, and dust abundance, $[Z_{\rm D}/0.01] = [1]$. The dashed curves show $M_{\rm MIN}(\omega_\star)$ for models with, from bottom to top, different redshifts, $z_{\rm red} =$ 4, 6, and 8, but the same fiducial dust abundance, i.e. $[Z_{\rm D}/0.01] = [1]$. The dotted curves show $M_{\rm MIN}(\omega_\star)$ for models with, from bottom to top, different dust abundances. $[Z_{\rm D}/0.01] = [1/64]$, $[1/16]$, $[1/4]$, and $[4]$, but the same fiducial redshift, i.e. $z_{\rm red} = 0$. The ordinate is scaled logarithmically. The same line-styles and labelling system are used on Fig. 6, which shows the corresponding variations of $T_{\rm CRIT}$, $\bar{\tau}_{\rm CRIT}$, $R_{\rm CRIT}$, $\rho_{\rm CRIT}$, $P_{\rm CRIT}$, and $\Delta_{\rm CRIT}$.

depth, and the radius; the density stays approximately constant. The rate of increase of $M_{\rm MIN}$ with increasing $\omega_\star$ is very slow at low $\omega_\star$, but in the limit of high $\omega_\star$ ($\log_{10}(\omega_\star) \gtrsim -11$) the minimum mass increases approximately as

$$M_{\rm MIN} \simeq 120\,{\rm M}_\odot\,\omega_\star^{4/11}\,. \tag{22}$$

The dashed curves on Figs 5 and 6 show how the minimum mass varies with the suprathermal background if the dust abundance is held constant at its fiducial value, $[Z_{\rm D}/0.01] = [1]$, but different values are considered for the redshift (i.e. $z_{\rm red} = 2$, 4, 6, and 8). As already discussed in Section 4.1 (see equation 20), the higher the redshift (and hence the hotter and more intense the CMB), the stronger the suprathermal background has to be to contribute significant extra heating to the proto-fragment. Consequently the switch from $M_{\rm MIN}$ increasing very slowly with increasing $\omega_\star$ at low $\omega_\star$, to increasing very rapidly at high $\omega_\star$ occurs at

$$\omega_\star \gtrsim 5.6\times10^{-15}\,[1+z_{\rm red}]^4\,. \tag{23}$$

The dotted curves on Figs 5 and 6 show how the minimum mass varies with the suprathermal background if the redshift is held constant at its fiducial value, $z_{\rm red} = 0$, but different values are considered for the dust abundance (i.e. $[Z_{\rm D}/0.01] = [1/16]$, $[1/4]$, and $[4]$). Again there is a switch from a regime at low $\omega_\star$ where $M_{\rm MIN}$ increases very slowly with increasing $\omega_\star$ (because suprathermal radiation makes a very small contribution to the heating) to a regime

$$\omega_\star \gtrsim 2\times10^{-12}\left[\frac{Z_{\rm D}}{0.01}\right]^{-1}\,, \tag{24}$$

where suprathermal radiation makes the dominant contribution to the heating, and

$$M_{\rm MIN} \simeq 1.2\times10^4\,{\rm M}_\odot\,Z_{\rm D}\,\omega_\star^{4/11}\,. \tag{25}$$

There are similar changes to the temperature of the proto-fragment, its optical depth, and its radius; the density in the proto-fragment is approximately constant at $\sim 10^{-13}\,{\rm g\,cm^{-3}}$.

5 DISCUSSION

5.1 Overall trends

The minimum mass increases monotonically with increasing redshift ($\partial M_{\rm MIN}/\partial z_{\rm red} > 0$) (see Fig. 1), and with increasing suprathermal background ($\partial M_{\rm MIN}/\partial \omega_\star > 0$) (see Fig. 5), because the ambient radiation field is stronger – and in the case of redshift also hotter. The dependence on the dust abundance is a little more complicated, because there is in general a marginally optically thin regime in which high dust abundance promotes cooling and $M_{\rm MIN}$ is lower, and an optically thick regime in which high dust abundance inhibits cooling and $M_{\rm MIN}$ is higher. The rates of increase with redshift, $\partial M_{\rm MIN}/\partial z_{\rm red}$, and suprathermal background, $\partial M_{\rm MIN}/\partial \omega_\star$, switch from being very small to being large when (a) the associated radiation fields (CMB plus suprathermal) dominate the energy density, and (b) the dust emission is optically thick. There are three physical factors regulating this switch.

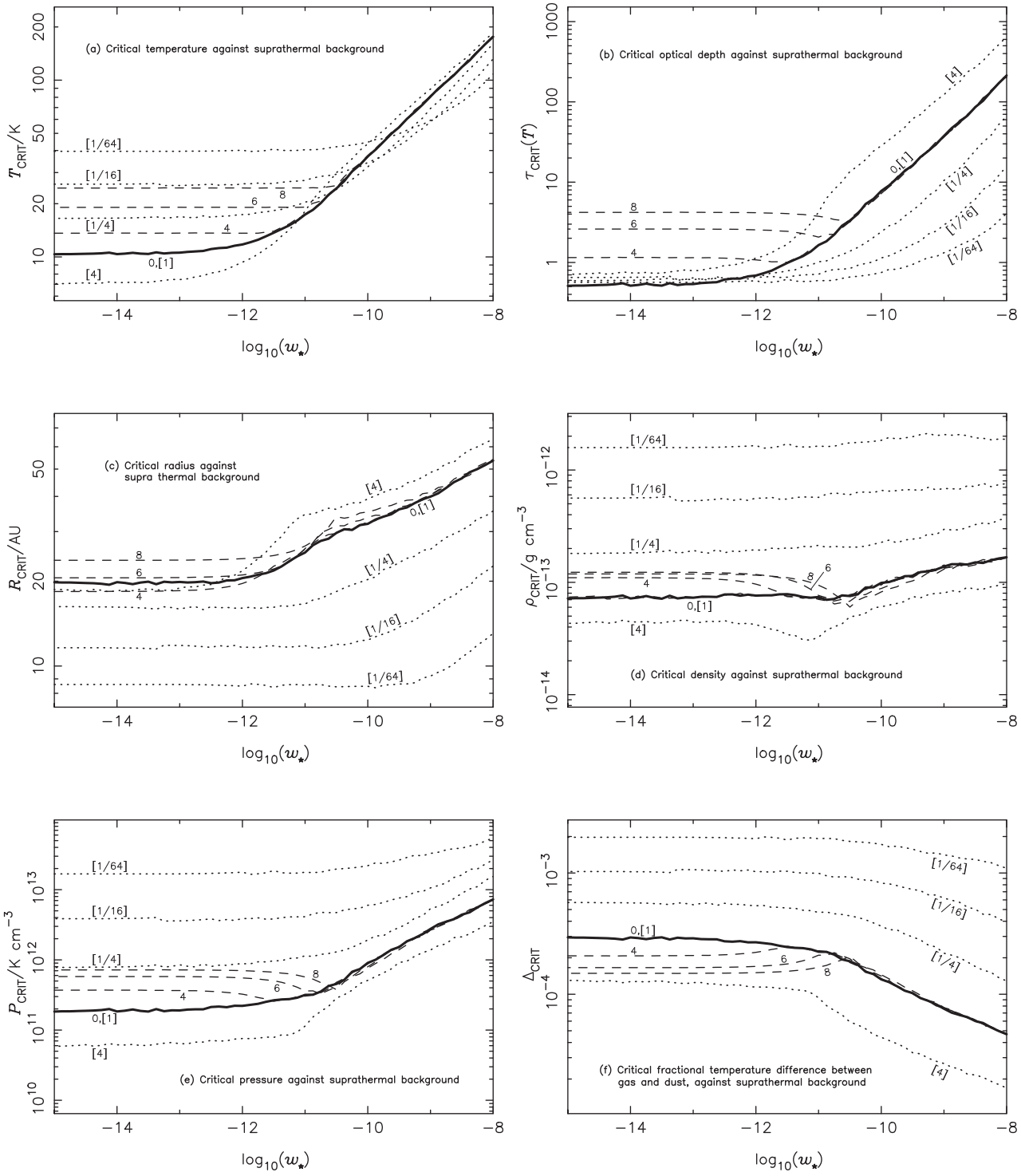

Figure 6. Plots showing the variation with suprathermal background, $\omega_\star$, of (a) the critical temperature, $T_{\rm CRIT}$, (b) the critical dust-emission optical depth, $\bar{\tau}_{\rm CRIT}$, (c) the critical radius, $R_{\rm CRIT}$, (d) the critical density, $\rho_{\rm CRIT}$, (e) the critical pressure, $P_{\rm CRIT}$, and (f) the critical fractional difference between the gas and dust temperatures, $\Delta_{\rm CRIT}$, for representative combinations of the redshift, $z_{\rm red}$, and the dust abundance, $Z_{\rm D}$. The full curve represents the fiducial combination, i.e. $z_{\rm red} = 0$ and $[Z_{\rm D}/0.01] = [1]$. The dashed curves show how the results change if the redshift is changed, i.e. i.e. $z_{\rm red} = 2$, 4, 6, and 8, but the dust abundance is held constant at $[Z_{\rm D}/0./01] = [1]$. The dotted curves show how the results change if the dust abundance is changed, i.e. $[Z_{\rm D}/0.01] = [1/16]$, [1/4], and [4], but the redshift is held constant at $z_{\rm red} = 0$. On all plots the ordinate is scaled logarithmically.

First, the conditions for the CMB to dominate (over the suprathermal background) *and* the dust emission to be optically thick are given by equations (20) and (21). This determines the region of parameter space where $\partial M_{\rm MIN}/\partial z_{\rm red}$ is large, principally due to the intensity of the CMB radiation field, and the trapping of cooling radiation.

Secondly, the conditions for the suprathermal background to dominate (over the CMB) *and* the dust emission to be optically thick are given by equations (23) and (24). This determines the region of parameter space where $\partial M_{\rm MIN}/\partial \omega_\star$ is large, principally due to the intensity of the suprathermal radiation field, and the trapping of cooling radiation.

Thirdly, below the switch the dust emission is only marginally optically thin, with an approximately universal effective optical depth, $\bar{\tau}_{\rm CRIT} \sim 0.7 \pm 0.2$. The temperature in the proto-fragment must be high enough that its energy density exceeds that of the ambient radiation field, but at the same time the optical depth adjusts so that the denominator in the dust cooling term (last term on the left-hand side of equation 17),

$$\mathcal{D}(T) = \bar{\tau}_{\rm RO}(T) + \bar{\tau}_{\rm PL}(T)^{-1}\,, \tag{26}$$

is close to its minimum, thereby giving the maximum cooling rate for this temperature, with an effective optical depth (equation 19)

$$\bar{\tau}_{\rm CRIT} \simeq [\bar{\tau}_{\rm PL}(T)/\bar{\tau}_{\rm RO}(T)]^{1/2}\,, \tag{27}$$

and $\bar{\tau}_{\rm RO}(T) \simeq [\bar{\tau}_{\rm RO}(T)/\bar{\tau}_{\rm PL}(T)]^{1/2}$, $\bar{\tau}_{\rm PL}(T) \simeq \bar{\tau}_{\rm RO}^{-1}(T) \simeq [\bar{\tau}_{\rm PL}(T)/\bar{\tau}_{\rm RO}(T)]^{1/2}$.

The consequent variation in the other parameters ($R_{\rm CRIT}, \rho_{\rm CRIT}, P_{\rm CRIT}$) follow from these constraints, and the requirement that the proto-fragment be marginally Jeans unstable and condensing at the sound speed.

Large (*vice* small) values of $M_{\rm MIN}$ always correlate with large (small) temperatures and large (small) optical depths, but there are no universal correlations between $M_{\rm MIN}$ and the radius, density, or pressure of the corresponding proto-fragment. This is again largely due to the non-linearity introduced by transfer of the cooling radiation against the dust optical depth, and its dependence on the dust abundance. For a marginally Jeans-unstable proto-fragment of given mass and radius (and therefore temperature), as the dust abundance is increased the cooling rate of the proto-fragment increases as long as it is in the optically thin regime, but once it becomes optically thick the rate decreases.

Proto-fragments corresponding to low values of $M_{\rm MIN}$ tend to be cool and marginally optically thin, because this maximizes their cooling rate. Proto-fragments corresponding to high values of $M_{\rm MIN}$ tend to be hot and optically thick.

Relatively large values of $M_{\rm MIN}$ are obtained at high redshift and high dust abundance (they are optically thick), but the highest values are obtained at high suprathermal background. The lowest values of $M_{\rm MIN}$ are obtained at low redshift, low suprathermal background, and high dust abundance (they are optically thin).

The parameter ranges are summarized in Table 1.

Table 1. Approximate ranges for the parameters adopted and predicted by our model.

Adopted parameter	Minimum	Maximum
Redshift, $z_{\rm red}$	0	8
Dust abundance, $Z_{\rm D}$	0.00016	0.04
Suprathermal background, $\omega_\star$	10^{-15}	10^{-8}
PREDICTED PARAMETER	MINIMUM	MAXIMUM
Minimum mass, $M_{\rm MIN}/[{\rm M}_\odot]$	0.0017	0.24
Temperature, $T_{\rm CRIT}/[{\rm K}]$	6.7	220
Dust-emission optical depth, $\bar{\tau}_{\rm CRIT}$	0.5	1000
Radius, $R_{\rm CRIT}/[{\rm au}]$	8	71
Density, $\rho_{\rm CRIT}/[{\rm g\,cm^{-3}}]$	10^{-14}	2×10^{-12}
Pressure, $P_{\rm CRIT}/[k_{\rm B}{\rm cm^{-3}\,K}]$	10^{10}	6×10^{13}
Fractional temperature difference, $\Delta_{\rm CRIT}$	0.00002	0.002

5.2 Comparison with other work

In this section, we compare our results with those of Li et al. (2023), Bate (2019), Bate (2023), and Chon et al. (2022). We must be mindful that our results are evaluated as a function of dust abundance, $Z_{\rm D}$,whereas all the results with which we compare them are expressed in terms of metallicity, $Z_{\rm met}$. To make comparisons, we assume that their $Z_{\rm met}$ is equal to twice our $Z_{\rm D}$, i.e. $Z_{\rm met} = 2Z_{\rm D}$.

5.2.1 Mass function of M Dwarfs as a function of metallicity and age

Based on a census of local M Dwarfs, Li et al. (2023) conclude that the proportion of low-mass stars in the interval $0.3\,{\rm M}_\odot$ to $0.7\,{\rm M}_\odot$ is lower in older populations, independent of metallicity. Qualitatively, this conforms with the results presented on Fig. 1. At all metallicities, we find that the minimum mass, $M_{\rm MIN}$, increases with redshift, $z_{\rm red}$, as shown by the bold and dashed curves on Fig. 1. Therefore, as we sample older populations, we expect the proportion of stars at the lower end of the interval to fall relative to the proportion at the upper end, in accordance with the findings of Li et al. (2023).

However, these increases are only significant when we enter the optically thick regime. For the fiducial dust abundance, $Z_{\rm met} = 0.02$, and the fiducial (and negligible) suprathermal background, $\omega_\star = 10^{-14}$, this means $z_{\rm red} \gtrsim 4$, or equivalently a look-back time more than 90 per cent of the age of the Universe. For lower metallicities the look-back time is even longer, so unless the local Milky Way contains a significant population of stars that are both very old, and quite metal rich, our estimates do not provide a viable explanation for Li et al.'s observations.

5.2.2 Detailed numerical simulations of star formation at low redshifts and high metallicities

Our results can also be compared with the smoothed particle hydrodynamics (SPH) simulations reported by Bate (2019) and Bate (2023), since these specifically predict the distribution of masses for different redshifts, $z_{\rm red}$, and different metallicities, $Z_{\rm met}$.

At the current epoch, $z_{\rm red} = 0$, Bate (2019) finds that the minimum mass is approximately independent of metallicity, with $M_{\rm MIN} \sim 0.010\,{\rm M}_\odot$. We find somewhat lower values, and a slow but steady decrease with increasing metallicity, from $\sim 0.007\,{\rm M}_\odot$ at $Z_{\rm met} = 0.0002$ to $\sim 0.003\,{\rm M}_\odot$ at $Z_{\rm met} = 0.06$, as shown by the bold curve on Fig. 3 and recorded in Table 2.

At redshift $z_{\rm red} = 5$, Bate (2023) finds a rather high minimum mass, $M_{\rm MIN} \sim 0.100\,{\rm M}_\odot$ at low metallicity, $Z_{\rm met} = 0.0002$. At higher metallicities, $0.002 \lesssim Z_{\rm met} \lesssim 0.02$, he again finds values $M_{\rm MIN} \sim 0.010\,{\rm M}_\odot$, close to those he finds at $z_{\rm red} = 0$. At this redshift we find values of $M_{\rm MIN} \sim 0.007\,{\rm M}_\odot$ that are almost independent $Z_{\rm met}$.

There does not appear to be a physical reason for a floor at $\sim 0.010\,{\rm M}_\odot$. Indeed one would expect $M_{\rm MIN}$ to decrease with decreasing redshift, due to the decrease in the temperature of the CMB (from $T_{\rm CMB} \simeq 16.4\,{\rm K}$ at $z_{\rm red} = 5$ to $T_{\rm CMB} \simeq 2.73\,{\rm K}$ at $z_{\rm red} = 0$). One might also expect $M_{\rm MIN}$ to decrease with increasing metallicity for contemporary star formation ($z_{\rm red} = 0$), since in the

Table 2. Comparison of our predictions with those of Bate (2019, 2023). The first three columns give the redshift, $z_{\rm red}$, the metallicity, $Z_{\rm met}$, and the corresponding dust abundance, on the assumption that $Z_{\rm D} = Z_{\rm met}/2$. The last two columns give the minimum masses obtained by Bate (2019, 2023), and those obtained by us. All values are given to one significant figure.

$z_{\rm red}$	$Z_{\rm met}$	$Z_{\rm D}$	$M_{\rm MIN:\,B}/{\rm M}_\odot$	$M_{\rm MIN:\,W}/{\rm M}_\odot$
0	0.0002	0.0001	0.010	0.007
0	0.002	0.001	0.010	0.006
0	0.02	0.01	0.010	0.004
0	0.06	0.03	0.010	0.003
5	0.0002	0.0001	0.100	0.007
5	0.002	0.001	0.010	0.006
5	0.02	0.01	0.010	0.006

optically thin regime increased metallicity will increase the cooling rate. Furthermore, there is growing observational evidence for free-floating objects with masses well below $0.010\,{\rm M}_\odot$, as discussed in the introduction.

The divergence between our predictions and the simulations is quite small (less than, or of the order of, a factor of 2), and may be attributable to the limitations of the one-zone model, or to the limitations of the SPH simulations, or both. The obvious limitation of the one-zone model is that it does not include rotation. In reality, and in the simulations, proto-fragments will be created with finite angular momentum, and this will inhibit contraction, thereby increasing the minimum mass. However, there will be circumstances under which a proto-fragment is created with negligible angular momentum, and this will be a requirement to realize the minimum mass. It is therefore worth considering the effects that might influence the ability of SPH simulations to form very low-mass stars.

Firstly, the condition for merging sink particles in the SPH simulations will preferentially remove the lower mass stars, since they will tend to be born in closer proximity to one another than more massive stars (because at their inception they have smaller intrinsic sizes).

Secondly, SPH simulations have limited mass resolution, and capturing the circumstances producing the minimum mass tests those limitations particularly strongly. This is because a minimum-mass proto-fragment must separate from a background with comparable density, and therefore some SPH particles in the proto-fragment inevitably have neighbours outside the fragment, and *vice versa*. Individual SPH particles in the Bate (2019, 2023) simulations have mass $m_{\rm SPH} \simeq 1.4 \times 10^{-5}\,{\rm M}_\odot$. For a proto-fragment that is just starting to separate out from a more extended medium, it is reasonable to assume uniform density. A proto-fragment with mass $\sim 0.010\,{\rm M}_\odot$ then contains ∼700 SPH particles, their kernels have radii $r_{\rm K} \sim 0.43R$, and so ∼ 82 per cent of the SPH particles in the proto-fragment overlap its boundary. If we consider a smaller proto-fragment with mass $\sim 0.003\,{\rm M}_\odot$ it contains only ∼210 SPH particles, their kernels have radii $r_{\rm K} \sim 0.65R$, and so ∼ 96 per cent of the SPH particles in the proto-fragment overlap its boundary.

Thirdly, the number of stars produced in the simulations is small, typically of order 100. If the Bate mass functions are approximately log-normal, and $\log_{10}(M_\star/{\rm M}_\odot)$ has a mean of $\mu_{\rm B}$ and a standard deviation of $\sigma_{\rm B}$, we should only expect one star in a hundred below

$$M_{1\ {\rm per\ cent}} = 10^{\mu_{\rm B} - 2.326\sigma_{\rm B}}\,{\rm M}_\odot. \tag{28}$$

Table 3 gives values of $M_{1\ {\rm per\ cent}}$ for different $\sigma_{\rm B}$, assuming $\mu_{\rm B} \simeq -0.82$, the smallest value reported by Bate (2023). The standard deviation of the log-normal distribution presented by Chabrier (2003) for the field is $\sigma_{\rm C} = 0.69$, and presumably this is an average over a range of different star-formation environments. In contrast, the Bate simulations explore a single realization of a particular cloud, so we should expect them to have lower $\sigma_{\rm B}$. The values in Table 3 imply that forming stars significantly below $\sim 0.010\,{\rm M}_\odot$ may be rare in the simulations, simply on statistical grounds, unless $\sigma_{\rm B} \gtrsim \sigma_{\rm C}$, which seems unlikely.

Table 3. Constraints on the standard deviation of log-normal IMFs. All IMFs are presumed to have mean $\mu_{\rm B} = -0.82$ (the lowest value reported by Bate 2019, 2023). The first row then gives possible values of the standard deviation, $\sigma_{\rm B}$, and the second row gives the mass, $M_{1\ {\rm per\ cent}}$, below which one should expect one out of 100 stars.

$\sigma_{\rm B}$	0.30	0.40	0.50	0.60	0.70
$M_{1\%}/{\rm M}_\odot$	0.0304	0.0178	0.0104	0.0061	0.0036

5.2.3 *Detailed numerical simulations of star formation at high redshifts and low metallicities*

Chon et al. (2022) have also used SPH simulations to explore how the IMF varies with redshift and metallicity, but in the main they are concerned with more extreme (larger) redshifts, and more extreme (lower) metallicities than us, specifically $0 \le z_{\rm red} \le 20$ and $2 \times 10^{-6} \le Z_{\rm met} \le 2 \times 10^{-3}$. They show that increasing the temperature of the CMB (i.e. increasing the redshift, $z_{\rm red}$) reduces the proportion of low-mass stars when the metallicity is relatively high, $Z_{\rm met} \gtrsim 0.01$, but has less effect when it is low, $Z_{\rm met} \lesssim 0.001$. Minimum masses are typically in the range 0.003 to $0.010\,{\rm M}_\odot$.

Our results only extend down to metallicity $Z_{\rm met} = 0.00032$, and up to redshift $z_{\rm red} = 8$, but the values of $M_{\rm MIN}$ obtained, and their variation with $Z_{\rm met}$ and $z_{\rm red}$ are in reasonable agreement (within 50 per cent) with the Chon et al. (2022) results, both in terms of absolute values, and as regards the trends with increasing metallicity and/or redshift. At our lowest metallicity $Z_{\rm met} = 0.00032$, $M_{\rm MIN}$ is essentially independent of $z_{\rm red}$, between $z_{\rm red} = 0$ and $z_{\rm red} = 8$. At higher metallicities, $M_{\rm MIN}$ is slightly lower at low $z_{\rm red}$, but then increases with $z_{\rm red}$ at higher values of $z_{\rm red}$.

5.3 Effect of changing $M_{\rm MIN}$ on the IMF

Although individual stars very close to the minimum mass are unlikely to play a crucial role in determining the structure, evolution, and appearance of the Universe, systematic changes in the minimum mass are likely to be reflected in the overall stellar IMF. In particular, an increase in the minimum mass should result in a more bottom-light IMF and a lower mass-to-light ratio, all other things being equal. Conversely, a reduction in the minimum mass should result in a more bottom-heavy IMF and a higher mass-to-light ratio, all other things being equal. On galactic scales, this will have implications for the build-up of heavy elements in the interstellar medium, for the evaluation of overall star formation rates in other galaxies, and for the likelihood of main-sequence stars from earlier epochs surviving to the present day. We attempt to evaluate the effect of changing $M_{\rm MIN}$ on the IMF in Appendix F.

6 CONCLUSIONS

(i) We have constructed a simple one-zone model for a proto-fragment that is heated by compression, by the CMB, and by suprathermal radiation (e.g. from nearby hot stars and sources of cosmic rays); it is cooled by thermal dust emission.

(ii) This enables us to formulate an approximate analytic expression for the net heating rate, and hence to determine the minimum mass of a proto-fragment that can condense out as a star.

(iii) The proto-fragment defining the minimum mass is marginally Jeans-unstable, contracts just fast enough to separate from its surroundings (i.e. at the sound speed), and has a net cooling rate due to dust emission that is just positive.

(iv) The minimum mass is determined by

(a) the redshift, $z_{\rm red}$ (which determines the temperature of the CMB),

(b) the dust abundance, $Z_{\rm D}$ (which determines the mass-opacity coefficient), and

(c) the dilution factor for the suprathermal background, $\omega_\star$ (which determines the strength of the ambient short-wavelength radiation field).

(v) For the ranges of redshift, dust abundance, and suprathermal background considered here – respectively $0 \lesssim z_{\rm red} \lesssim 8$, $0.00016 \lesssim Z_{\rm D} \lesssim 0.04$, $10^{-15} \lesssim \omega_\star \lesssim 10^{-8}$ – values of $M_{\rm MIN}$ fall in the range $0.002\,{\rm M}_\odot \lesssim M_{\rm MIN} \lesssim 0.2\,{\rm M}_\odot$.

(vi) Our results agree quite well with results obtained from detailed numerical simulations (Bate 2019, 2023; Chon et al. 2022), but are somewhat lower; the numerical simulations may be slightly compromised by resolution effects and/or small-number statistics.

(vii) Increases in the minimum mass are usually accompanied by an increase in the temperature and optical depth of the proto-fragment.

(viii) We have shown that the pressure in a minimum-mass proto-fragment is always sufficiently high that the gas-kinetic and dust-vibrational temperatures are very close (see Appendix C).

(ix) Increases in the minimum mass may deliver a significantly bottom-light IMF, and hence a greatly reduced mass-to-light ratio.

(x) The largest $M_{\rm MIN}$ values are obtained when there is a strong suprathermal background radiation field, as for example in a galactic nucleus; this may have serious consequences for the mass-to-light ratios of such regions and the development of their metal abundances.

ACKNOWLEDGEMENTS

APW gratefully acknowledges the support of an STFC Consolidated Grant (ST/K00926/1). RW and JP acknowledge support by the institutional project RVO:67985815.

DATA AVAILABILITY

All software used will be supplied on request to APW.

REFERENCES

Bate M. R., 2005, MNRAS, 363, 363
Bate M. R., 2019, MNRAS, 484, 2341
Bate M. R., 2023, MNRAS, 519, 688
Boss A. P., 1988, ApJ, 331, 370
Boyd D. F. A., Whitworth A. P., 2005, A&A, 430, 1059
Chabrier G., 2003, PASP, 115, 763
Chon S., Ono H., Omukai K., Schneider R., 2022, MNRAS, 514, 4639
Clark C. J. R., Roman-Duval J. C., Gordon K. D., Bot C., Smith M. W. L., Hagen L. M. Z., 2023, ApJ, 946, 42
De Vis P. et al., 2019, A&A, 623, A5
Forgan D., Rice K., 2013, MNRAS, 432, 3168
Galliano F. et al., 2021, A&A, 649, A18
Goswami S. et al., 2022, A&A, 663, A1
Hollenbach D., McKee C. F., 1979, ApJS, 41, 555
Hoyle F., 1953, ApJ, 118, 513
Hu C.-Y., Sternberg A., van Dishoeck E. F., 2023, ApJ, 952, 140
Konstantopoulou C. et al., 2024, A&A, 681, A64
Li J., Liu C., Zhang Z.-Y., Tian H., Fu X., Li J., Yan Z.-Q., 2023, Nature, 613, 460
Lodieu N., Dobbie P. D., Cross N. J. G., Hambly N. C., Read M. A., Blake R. P., Floyd D. J. E., 2013, MNRAS, 435, 2474
Lodieu N., Hambly N. C., Cross N. J. G., 2021, MNRAS, 503, 2265
Lomax O., Whitworth A. P., Hubber D. A., 2016, MNRAS, 458, 1242
Low C., Lynden-Bell D., 1976, MNRAS, 176, 367
Machida M. N., Inutsuka S.-i., Matsumoto T., 2009, ApJ, 699, L157
Masunaga H., Inutsuka S.-i., 1999, ApJ, 510, 822
Mathis J. S., 1990, ARA&A, 28, 37
Pearson S. G., McCaughrean M. J., 2023, preprint (arXiv:2310.01231)
Rees M. J., 1976, MNRAS, 176, 483
Reipurth B., Clarke C., 2001, AJ, 122, 432
Salpeter E. E., 1955, ApJ, 121, 161
Sharda P., Amarsi A. M., Grasha K., Krumholz M. R., Yong D., Chiaki G., Roy A., Nordlander T., 2023, MNRAS, 518, 3985
Silk J., 1977, ApJ, 214, 152
Smith R. C., 1977, MNRAS, 179, 521
Smith R. C., Wright A. E., 1975, MNRAS, 172, 221
Spitzer L., 1978, Physical Processes in the Interstellar Medium. Wiley, New York
Stamatellos D., Whitworth A. P., 2009, MNRAS, 392, 413
Whitworth A., 1981, MNRAS, 195, 967
Whitworth A. P., 2018, in Deeg H. J., Belmonte J. A., eds, Handbook of Exoplanets. Springer, Heidelberg, p. 95
Whitworth A., Lomax O., 2016, Publ. Astron. Soc. Aust., 33, e003
Whitworth A. P., Stamatellos D., 2006, A&A, 458, 817
Whitworth A. P., Zinnecker H., 2004, A&A, 427, 299
Whitworth A., Bate M. R., Nordlund Å., Reipurth B., Zinnecker H., 2007, in Reipurth B., Jewitt D., Keil K., eds, Protostars and Planets V. University of Arizona Press, Tucson, p. 459
Yang R.-z., Li G.-X., Wilhelmi E. d. O., Cui Y.-D., Liu B., Aharonian F., 2023, Nat. Astron., 7, 351

APPENDIX A: THE PLANCK- AND ROSSELAND-MEAN OPACITIES

The Planck- and Rosseland-mean dust opacities have been computed using monochromatic opacities, κ_λ, derived from the relative extinction values, $A_\lambda/A_{\rm J}$, tabulated by Mathis (1990). We adopt his values for total to selective extinction $R_{\rm V} = 5.0$, since these probably represent better the dust in a pre-stellar core. We do not distinguish the absorption and scattering contributions to extinction, because we are mainly concerned with radiation having temperature $\lesssim 70\,{\rm K}$, and therefore with long wavelengths, $\gtrsim 10\,\mu{\rm m}$ where extinction is dominated by absorption.

The only place where the distinction between scattering and absorption will have an impact on the transport of radiation is the dust jacket around a proto-fragment where the ambient suprathermal radiation field is thermalized (see Appendix C). However, we only need to demonstrate that absorption of suprathermal radiation in this jacket involves a very small column-density of dust, as compared with the column-density through the actual proto-fragment. This issue is dealt with in Appendix B5.

The Planck-mean opacity is given by

$$\bar{\kappa}_{\rm PL}(T) \;=\; \frac{15}{\pi^4}\int_{\lambda=0}^{\lambda=\infty} \frac{[hc/\lambda k_{\rm B}T]^4\;\kappa_\lambda\;d\ln\lambda}{\{\exp[hc/\lambda k_{\rm B}T]-1\}};$$

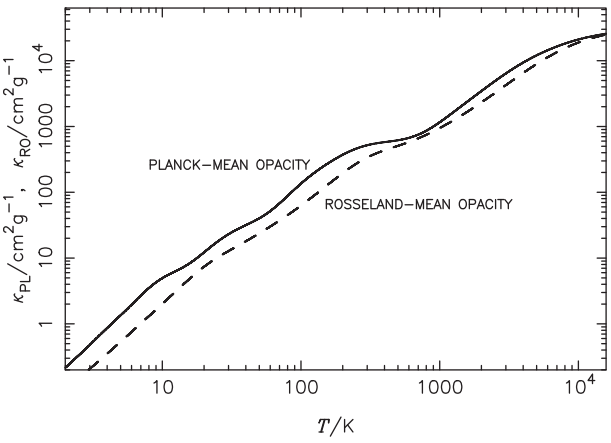

Figure A1. The Planck- and Rosseland-mean opacities.

and the Rosseland-mean opacity by

$$\frac{1}{\bar{\kappa}_{\rm RO}(T)} = \frac{15}{4\pi^4}\int_{\lambda=0}^{\lambda=\infty}\frac{[hc/\lambda k_{\rm B}T]^5\,\exp[hc/\lambda k_{\rm B}T]\;d\ln\lambda}{\{\exp[hc/\lambda k_{\rm B}T]-1\}^2\;\kappa_\lambda};$$

The results are plotted on Fig. A1. The full curve represents the Planck-mean opacity. The dashed curve represents the Rosseland-mean opacity.

APPENDIX B: APPROXIMATE EXPRESSIONS FOR EXCHANGE OF RADIATION BETWEEN THE PROTO-FRAGMENT AND ITS SURROUNDINGS

In this appendix we unpack some of the terms in the energy equation (equation 4).

B1 The dust cooling term in equation 4

First, we consider dust cooling in the optically thin limit. The dust-emission luminosity of the proto-fragment is

$$\Lambda_{\rm D:THIN} \simeq M_{\rm O}4\bar{\kappa}_{\rm PL}(T)\sigma_{\rm SB}T^4 \simeq 4\pi R^2\sigma_{\rm SB}T^4\,\bar{\tau}_{\rm PL}(T). \quad \text{(B1)}$$

Secondly, we consider dust cooling in the optically thick limit. The amount of radiant energy in the proto-fragment is $U_{\rm RAD} \simeq 16\pi R^3\sigma_{\rm SB}T^4/3c$, and the mean-free-path for this radiation is $\bar{\ell} \simeq 4\pi R^3/3M_{\rm O}\bar{\kappa}_{\rm RO}(T)$. Consequently this radiation requires of order $[R/\bar{\ell}]^2$ free paths to diffuse to the surface by a random walk. Since each free path takes a time $\sim[\bar{\ell}/c]$, the radiation escapes on a time-scale is $\sim t_{\rm DIFF} \sim [R/\bar{\ell}]^2[\bar{\ell}/c] = R^2/\bar{\ell}c$, and the dust-emission luminosity is

$$\Lambda_{\rm D:THICK} \simeq \frac{U_{\rm RAD}}{t_{\rm DIFF}} \sim \frac{4\pi R^2\sigma_{\rm SB}T^4}{\bar{\tau}_{\rm RO}(T)}. \quad \text{(B2)}$$

If we now write

$$\Lambda_{\rm D} \sim \frac{4\pi R^2\sigma_{\rm SB}T^4}{\bar{\tau}_{\rm RO}(T)+\bar{\tau}_{\rm PL}^{-1}(T)}, \quad \text{(B3)}$$

then in the optically thin limit, $\bar{\tau}_{\rm PL}(T) \ll 1$ (and $\bar{\tau}_{\rm RO}(T) \ll 1$, since the Planck- and Rosseland-mean opacities never differ by more than a factor ~2) we recover equation (B1). Conversely, in the optically thick limit, $\bar{\tau}_{\rm RO}(T) \gg 1$ (and therefore $\bar{\tau}_{\rm PL}(T) \gg 1$) we recover equation (B2). equation (B3) is the radiative dust cooling term in equation (4) (the final term on the right-hand side).

B2 The effective temperature of the dust cooling emission

We stress that T is the *mean internal temperature* of the dust and gas in the proto-fragment.

From equation (4), if the proto-fragment is optically thin ($\bar{\tau}_{\rm PL}(T) < 1$), the flux of dust cooling radiation from its surface is

$$F_{\rm DUST:THIN} \sim \sigma_{\rm SB}T^4\bar{\tau}_{\rm PL}(T), \quad \text{(B4)}$$

and the effective temperature of this cooling radiation is

$$T_{\rm EFF:THIN} \simeq 1.3T. \quad \text{(B5)}$$

The 30 per cent fractional increase in the effective temperature is due to the wavelength dependence of the dust opacity, which we assume to be characterized by an emissivity index $\beta = -{\rm dln}(\kappa_\lambda)/{\rm dln}(\lambda) \sim 2$.

Similarly, from equation (4), if the proto-fragment is optically thick, ($\bar{\tau}_{\rm RO}(T) > 1$), the flux of dust cooling radiation from its surface is

$$F_{\rm DUST:THICK} \sim \sigma_{\rm SB}T^4/\bar{\tau}_{\rm RO}(T). \quad \text{(B6)}$$

In this optically thick limit, the flux of dust cooling radiation from the surface of the proto-fragment can also be expressed in terms of an effective temperature, $T_{\rm EFF:\,THICK}$, *viz.*

$$F_{\rm DUST:THICK} \sim \sigma_{\rm SB}T_{\rm EFF:THICK}^4. \quad \text{(B7)}$$

Equating the right-hand sides of equations (B6) and (B7), we obtain

$$T_{\rm EFF:THICK} \simeq \bar{\tau}_{\rm RO}^{-1/4}(T)\;T\,. \quad \text{(B8)}$$

B3 The CMB heating term in equation (4)

Next consider a hypothetical situation in which the proto-fragment is static and only heated by the CMB. Since the CMB is, to a high degree of accuracy, a blackbody radiation field, the dust must must come into thermal equilibrium with the CMB at $T \simeq T_{\rm CMB}$. This must be true for any value of $T_{\rm CMB}$, so by the Principle of Detailed Balance, the form of the term for the CMB heating rate must be the same as that for the dust-emission luminosity (equation B3), but with $T_{\rm CMB}$ in place of T, i.e.

$$\Gamma_{\rm CMB} \sim \frac{4\pi R^2\sigma_{\rm SB}T_{\rm CMB}^4}{\bar{\tau}_{\rm RO}(T_{\rm CMB})+\bar{\tau}_{\rm PL}^{-1}(T_{\rm CMB})}. \quad \text{(B9)}$$

Moreover, since the *monochromatic* dust opacity κ_λ (as distinct from the Rosseland- and Planck-mean opacities) is presumed here to be independent of temperature, this must still hold when other heating terms are included. Equation (B9) is the CMB heating term in equation (4) (the second term on the right-hand side).

B4 The heating term due to the suprathermal background in equation (4)

To formulate the heating term due to the suprathermal background, $\Gamma_\star$, we must take account of the fact that the energy equation (equation 4) deals with heating throughout the entire interior of the proto-fragment (e.g. due to compression and the CMB), and with cooling from the entire interior of the proto-fragment (due to emission and diffusive transport of radiation by dust).

A simple procedure for estimating the heating rate due to the suprathermal background must take account of the fact that a minimum-mass proto-fragment is always optically thick to the suprathermal background, as shown in Appendix B5. Consequently most of the suprathermal background radiation is absorbed in a

very thin shell at the surface of the proto-fragment (hereafter 'Shell 1'), and re-emitted at longer wavelengths. Some of this re-emitted radiation then penetrates further into the proto-fragment, where most of it will be absorbed in 'Shell 2' and re-emitted at even longer wavelengths. For a sufficiently surface-dense proto-fragment and a sufficiently intense suprathermal background, this process of absorption and re-emission, with steady degradation of the wavelength, repeats recursively until the radiation reaches the centre of the proto-fragment.

Now consider a proto-fragment with mass $M_{\rm O}$, radius R, and uniform density ρ. Suppose that the proto-fragment is broken up into nested spherically symmetric shells, labelled (from the outside inwards) $n = 1, 2, 3$, etc. The radial range of Shell 1 is $r_1 < r \leq R$; the radial range of Shell 2 is $r_2 < r \leq r_1$; the radial range of Shell 3 is $r_3 < r \leq r_2$; and so on. We assume that each shell only exchanges radiant energy with its neighbours, and that the Rosseland-mean dust opacity varies as $\bar{\kappa}_{\rm RO}(T) \propto T^{\,\beta}$ across the entire dust-temperature range. We could use the detailed opacities calculated in Section A, but this would incur a large computational penalty in the procedure we describe below, and the above approximation with $\beta = 5/4$ is a good fit to the opacities plotted on Fig. A1.

For Shell 1, there is an external flux of suprathermal (therefore short-wavelength) radiation,

$$F_\star = \omega_\star \, \sigma_{\rm SB} \, T_\star^{\,4} \,, \tag{B10}$$

incident on the outer boundary of Shell 1, and we assume (a) that all this energy is absorbed in Shell 1, and (b) that Shell 1 is optically thick and geometrically thin. The thickness of Shell 1 is therefore given approximately by

$$[R - r_1] \, \bar{\kappa}_{\rm RO}(T_0) \, \rho \simeq 1 \,, \tag{B11}$$

so

$$r_1 \simeq R \, - \, \bar{\ell}_0 \,, \tag{B12}$$

$$\bar{\ell}_0 = [\bar{\kappa}_{\rm RO}(T_0)\rho]^{-1} \,. \tag{B13}$$

The dust-temperature in Shell 1 is given approximately by

$$\bar{\kappa}_{\rm RO}(T_\star) \, \omega_\star \, T_\star^{\,4} \simeq 2 \, \bar{\kappa}_{\rm RO}(T_1) \, T_1^{\,4} \,. \tag{B14}$$

Here the factor of 2 takes account of the fact that the shell is only irradiated from the outside but emits in all directions. From equation (B14) we obtain

$$T_1 \simeq \left[\frac{\omega_\star}{2} \right]^{1/[4+\beta]} T_\star \,. \tag{B15}$$

For Shell 2, the external flux of radiation incident on the boundary of Shell 2 is the inward emission from shell 1, i.e.

$$F_2 \simeq \omega_1 \, \sigma_{\rm SB} \, T_1^{\,4} \quad \simeq \quad \frac{\omega_\star}{2} \, \sigma_{\rm SB} \, T_\star^{\,4} \,, \tag{B16}$$

so

$$\omega_1 \simeq \frac{\omega_\star}{2} \left[\frac{T_1}{T_\star} \right]^{-4} \,. \tag{B17}$$

The thickness of Shell 2 is given by

$$[r_1 - r_2] \, \bar{\kappa}_{\rm RO}(T_1) \rho \simeq 1 \,, \tag{B18}$$

where

$$r_2 \simeq r_1 \, - \, \left[\frac{T_1}{T_\star} \right]^{-\beta} \bar{\ell}_0 \,. \tag{B19}$$

The dust-temperature in Shell 2 is given approximately by

$$\bar{\kappa}_{\rm RO}(T_1) \, \omega_1 \, T_1^{\,4} \simeq 2 \, \bar{\kappa}_{\rm RO}(T_2) \, T_2^{\,4} \,, \tag{B20}$$

which reduces to

$$T_2 \simeq \left\{ \frac{\omega_0 \, T_\star^{\,4} \, T_1^{\,\beta}}{2^2} \right\}^{1/[4+\beta]} \,. \tag{B21}$$

For each shell we assume that the outward emission escapes freely from the proto-fragment, but the inward emission is absorbed in the next shell. This is qualitatively correct because the wavelength is degraded from each shell to the next, and therefore the associated opacity decreases and the surface-density increases.

For general Shell n, the radius and temperature are given by the recurrence relations

$$r_n = r_{n-1} \, - \, \left[\frac{T_{n-1}}{T_\star} \right]^{-\beta} \bar{\ell}_0 \,, \tag{B22}$$

$$T_n = \left\{ \frac{\omega_0 \, T_\star^{\,4} \, T_{n-1}^{\,\beta}}{2^n} \right\}^{1/[4+\beta]} \,, \tag{B23}$$

and shells are generated until the innermost shell is found with

$$r_N \leq 0 \,. \tag{B24}$$

The total heating rate due to suprathermal radiation is then obtained by summing the contributions from the different shells, which reduces to

$$\Gamma_\star(\omega_\star, M_{\rm O}, R) \simeq 4 \, \pi \, \omega_\star \, \sigma_{\rm SB} \, T_\star^{\,4} \left[R^2 \, + \, \sum_{n=1}^{n=N} \left\{ \frac{r_n^2}{2^n} \right\} \right] . \tag{B25}$$

B5 Typical optical depths

To demonstrate that the proto-fragment is always optically thick to the suprathermal background radiation, we reference Table 1 and Fig. A1. From Table 1 we have $T \lesssim 200\,{\rm K}$, and therefore from Fig. A1

$$\left. \frac{\bar{\tau}_{\rm RO}(T_\star)}{\bar{\tau}_{\rm RO}(T)} \right|_{\rm CRIT} \simeq \frac{\bar{Q}_{\rm D}(T_\star = 10^4 {\rm K})}{\bar{Q}_{\rm D}(T \lesssim 200\,{\rm K})} \quad \gtrsim \quad 50 \,. \tag{B26}$$

From Table 1 we have $\bar{\tau}_{\rm CRIT} \gtrsim 0.5$, and therefore the optical depth presented to the incident suprathermal radiation is $\bar{\tau}_{\rm RO}(T_\star) \gtrsim 25$; usually it is significantly larger than this.

This means that there should be a small skin around the proto-fragment where molecules are dissociated, and also possibly atoms are ionized. We can neglect this for two reasons. First, the skin is very thin. Secondly, dissociation/ionization only affects the mean gas-particle mass, $\bar{m}_{\rm O}$, and as we discuss in Section 2.1 and Appendix D this has at most a very small effect on the minimum mass.

APPENDIX C: THERMALIZATION OF GAS AND DUST

We have assumed that the difference between the gas-kinetic temperature and the dust-vibrational temperature can be neglected. This requires that exchange of thermal energy between the gas and the dust is very rapid. Specifically, if the dust temperature is given by $T_{\rm D} = T[1 - \Delta]$, we require that

$$|\Delta| \, = \, \left| \frac{[T - T_{\rm D}]}{T} \right| \quad \ll \quad 1. \tag{C1}$$

The rate of transfer of thermal energy from gas to dust is

$$\Lambda_{\rm GD} \, \simeq \, 3 \left[\frac{2}{\pi} \right]^{1/2} \rho \, \left[\frac{k_{\rm B} T}{\bar{m}_{\rm O}} \right]^{3/2} \kappa_{\rm O}(Z_{\rm D}) \, \alpha_{\rm D}(T) \, \Delta \tag{C2}$$

per unit mass, where $\alpha_D(T)$ is the accommodation coefficient. The temperatures involved here are mostly $T \lesssim 50\,\mathrm{K}$, and always $T \lesssim 200\,\mathrm{K}$, so we can set $\alpha_D \sim 1$ (e.g. Hollenbach & McKee 1979).

The gas heating rate per unit mass due to compression in freefall is

$$\Gamma_{FF} \simeq \left[\frac{k_B T}{\bar{m}_O}\right] \left[\frac{12\pi G\rho}{5}\right]^{1/2}. \tag{C3}$$

It follows that compressional heating of the gas can be exported from the proto-fragment by transferring heat to the dust (i.e. $\Lambda_{GD} \simeq \Gamma_{FF}$), provided the gas pressure $P = \rho k_B T/\bar{m}_O$, equals the thermalization pressure,

$$P_{THERM} \simeq \frac{2\pi^2 G}{15\,\kappa_O^2(Z_D)\,\Delta^2}. \tag{C4}$$

Substituting for $\kappa_O(Z_D)$ from equations (8) and (C4) reduces to

$$P_{THERM} \simeq \frac{2.2\times10^{-16}\,\mathrm{dyne\,cm^{-2}}}{Z_D^2\,\Delta^2} \tag{C5}$$

We can turn the requirement $P \simeq P_{THERM}$ around and compute the fractional temperature difference between the gas and the dust required for the compressional gas heating rate to be transferred to the dust (from where it can be radiated away),

$$\Delta \simeq \frac{1}{Z_D}\left[\frac{P}{2.2\times10^{-16}\,\mathrm{erg\,cm^{-3}}}\right]^{-1/2}. \tag{C6}$$

Δ_{CRIT} (the value of Δ in a proto-fragment at its inception) is plotted on Figs 2f, 4f, and 6f. For the minimum-mass proto-fragments analysed here, Δ is never above 0.002, so if, for example, the dust temperature were $T_D = 10.0\,\mathrm{K}$, the gas temperature would be in the range $10.00\,\mathrm{K} \le T \le 10.02\,\mathrm{K}$). Given the many other approximations made, it is acceptable to assume $T \simeq T_D$.

APPENDIX D: HOW THE MINIMUM MASS CHANGES IF WE ADOPT $Z_D = 0.5Z_{MET}$

We have repeated the computations presented in Sections 4.1 through 4.3, and in Figs 1 through 6, but with the relationship between metallicity and dust abundance (equation 3) replaced with the simpler relationship,

$$Z_{met} = 2\,Z_D. \tag{D1}$$

In other words, the results discussed in this appendix are based on the assumption that – independent of metallicity – half the metals are always in dust; consequently at lower dust abundance the metallicity is markedly lower here than has been assumed in the main body of the paper. We note that, because we have presented the results as a function of the dust abundance, changes in the metallicity only affect the results by altering the mean gas-particle mass ($\bar{m}_O$, see equation 1). This only changes the minimum mass significantly when *either* the redshift is low, $z_{red} \lesssim 6$, *or* the suprathermal background is weak, $\log_{10}(\omega_\star) \lesssim -12$, *or* both. Even under these circumstances, the minimum mass is only reduced by $\lesssim 5$ per cent.

APPENDIX E: HOW THE MINIMUM MASS CHANGES IF WE ADOPT FREEFALL COLLAPSE

We have also repeated the computations presented in Sections 4.1 through 4.3, and in Figs 1 through 6, but with the assumption that a proto-fragment can only separate out if it contracts at the freefall speed, rather than the sonic speed (see the formulation of Condition 2 in Section 3). This increases the compressional heating term in the energy equation (the first term in equation 17) by replacing $f_{SONIC} = 1$ with $f_{FREEFALL} = 10^{1/2}$. This increase in the compressional heating rate produces a ~ 100 per cent increase in the minimum mass (i.e. it is roughly doubled), under all circumstances. This approximately universal increase factor arises largely because, if the temperature is raised by a more intense cosmic-microwave or suprathermal background, the compressional heating rate is increased by a similar factor ($\propto T^{9/2}$) to the dust cooling rate ($\propto T^4$).

APPENDIX F: THE EFFECT OF THE MINIMUM MASS ON THE IMF

In order to estimate the influence of the minimum mass on the integral properties of the IMF – in particular the fraction of mass, $f(8\mathrm{M}_\odot)$, going into high-mass stars, $M > 8\,\mathrm{M}_\odot$ – we first characterize the current local IMF, using as few parameters as possible. Following the recent results of Pearson & McCaughrean (2023), we assume that the current local IMF is truncated at $M_{MIN:O} = 0.0007\,\mathrm{M}_\odot$.

Between $M_{MIN:O}$ and $M_S = 2.39\,\mathrm{M}_\odot$, we adopt a log-normal IMF with mean $M_C = 0.079\,\mathrm{M}_\odot$ and standard deviation $\sigma_C = 0.69$ (Chabrier 2003). Above M_S we adopt a power-law IMF with slope $\Gamma = 1.35$ (Salpeter 1955). The value of M_S is fit so that the IMF is continuous and smooth at M_S. The current local IMF, distinguished by subscript 0, is therefore given by

$$\left.\frac{d\mathcal{N}}{d\log_{10}(M)}\right|_0 = \begin{cases} 0, & M < M_{MIN:O}; \\ A_O \exp\left\{-\frac{\log_{10}^2(M/M_C)}{2\sigma_C^2}\right\}, & M_{MIN:O} < M < M_S; \\ 9.98\,A_O\,(M/M_C)^{-\Gamma}, & M > M_S. \end{cases} \tag{F1}$$

The current local IMF is plotted with a full curve on Fig. F1, where it has been normalized arbitrarily so that the net mass of stars is $10^3\,\mathrm{M}_\odot$. The fraction of mass going into stars more massive than $8\,\mathrm{M}_\odot$ is $f(8\mathrm{M}_\odot) \simeq 30$ per cent. The abrupt cut-off at M_{MIN} is unrealistic, but there is so little mass at this end of the IMF that cosmetically smoothing the abrupt cut-off would have little effect on any of the results presented below.

To estimate how the fraction of mass going into stars more massive than $8\,\mathrm{M}_\odot$ is affected by a change in M_{MIN}, we consider two extreme possibilities. For both possibilities, the IMF will – for the purpose of illustration and comparison – again be normalized so that the net mass of stars is $10^3\,\mathrm{M}_\odot$.

In the first possibility (labelled TRUNCATED), the IMF defined above (equation F1) is simply truncated below M_{MIN} instead of $M_{MIN:O}$. Provided that $M_{MIN} < M_S$, which is the case for all the values of M_{MIN} derived here, the TRUNCATED IMF is again given by equation (F1), but with $M_{MIN:O}$ replaced with M_{MIN}, i.e.

$$\left.\frac{d\mathcal{N}}{d\log_{10}(M)}\right|_T = \begin{cases} 0, & M < M_{MIN}; \\ A_T \exp\left\{-\frac{\log_{10}^2(M/M_C)}{2\sigma_C^2}\right\}, & M_{MIN} < M < M_S; \\ 9.98\,A_T\,(M/M_C)^{-\Gamma}, & M > M_S. \end{cases} \tag{F2}$$

Two examples of TRUNCATED IMFs are plotted with dashed curves on Fig. F1. These two examples are chosen so that $f(8\mathrm{M}_\odot)$ is 60 per cent and 90 per cent. It is clear that, for a TRUNCATED IMF, implausibly large values of M_{MIN} are required to significantly increase $f(8\mathrm{M}_\odot)$.

In the second possibility, which we label SHIFTED, the entire IMF is shifted to higher masses, by $\log_{10}(M_{MIN}/M_{MIN:O})$, so the SHIFTED IMF is given by equation (F1), but with M replaced with $M' = MM_{MIN:O}/M_{MIN}$, i.e.

$$\left.\frac{\mathrm{d}\mathcal{N}}{\mathrm{d}\log_{10}(M)}\right|_{\mathrm{S}} = \begin{cases} 0, & M' < M_{\mathrm{MIN}}; \\ A_{\mathrm{S}} \exp\left\{-\frac{\log_{10}^2(M'/M_{\mathrm{C}})}{2\sigma_{\mathrm{C}}^2}\right\}, & M_{\mathrm{MIN}} < M' < M_{\mathrm{S}}; \\ 9.98\, A_{\mathrm{S}}\, (M'/M_{\mathrm{C}})^{-\Gamma}, & M' > M_{\mathrm{S}}. \end{cases}$$
$$\text{with } M' = M M_{\mathrm{MIN:O}}/M_{\mathrm{MIN}}. \qquad \text{(F3)}$$

Two examples of SHIFTED IMFs are plotted with dotted curves on Fig. F1. These two examples are again chosen so that $f(8\mathrm{M}_\odot)$ is 60 per cent and 90 per cent. It is clear that, for a SHIFTED IMF, much smaller values of M_{MIN} are required to significantly increase $f(8\mathrm{M}_\odot)$.

On Fig. F2 we plot $f(8\mathrm{M}_\odot)$ against M_{MIN} for the two extreme types of IMF: TRUNCATED with a dashed curve, and SHIFTED with a dotted curve. This plot demonstrates that, on the basis of the estimates of M_{MIN} derived here, we cannot make a precise evaluation of how z_{red}, Z_{D}, and $\omega_\star$ affect $f(8\mathrm{M}_\odot)$. However, we can infer that increased M_{MIN} at high redshift and/or suprathermal background might dramatically increase $f(8\mathrm{M}_\odot)$.

With a TRUNCATED IMF, values of $M_{\mathrm{MIN}} \gtrsim 2\,\mathrm{M}_\odot$ are required to effect a significant increase in $f(8\mathrm{M}_\odot)$. Such values of M_{MIN} are well above the estimates made here, so if the TRUNCATED IMFs of equation (F2) are a good representation of what ensues when M_{MIN} is increased, there is unlikely to be a significant increase in $f(8\mathrm{M}_\odot)$ at higher redshift or suprathermal background. However, such an abrupt termination of the IMF seems unlikely, so this conclusion is extremely conservative.

With a SHIFTED IMF, values of $M_{\mathrm{MIN}} \gtrsim 0.003\,\mathrm{M}_\odot$ are sufficient to effect a significant increase in $f(8\mathrm{M}_\odot)$.[2] Such values of M_{MIN} are below most of the estimates made here, so if the SHIFTED IMFs of equation (F3) are a good representation of what ensues when M_{MIN} is increased, there is likely to be a significant increase in $f(8\mathrm{M}_\odot)$ at higher redshift or suprathermal background, and hence a lower mass-to-light ratio and important consequences for the mix of metals returned to the interstellar medium.

[2]The critical issue here is not the high-mass end of the IMF, where formally stars with $M \gtrsim 10^3\,\mathrm{M}_\odot$ are predicted but may not actually be able to form. The critical issue is whether the mass 'wasted' on low-mass stars can be significantly reduced.

This paper has been typeset from a TEX/LATEX file prepared by the author.

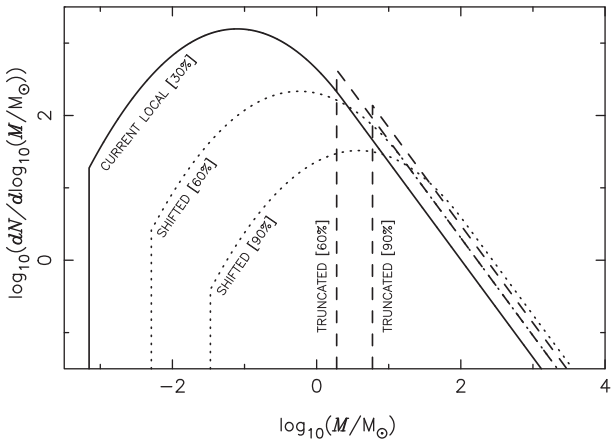

Figure F1. IMFs for different values of M_{MIN} and different assumptions about how the value of M_{MIN} affects the IMF at higher masses. The full curve is an approximation to the current local IMF (equation F1). The dashed curves represent TRUNCATED IMFs, i.e. the current local IMF truncated below M_{MIN}, for two different values of M_{MIN}, chosen so that they deliver $f(8\mathrm{M}_\odot) = 60$ per cent and 90 per cent (equation F2). The dotted curves represent SHIFTED IMFs, i.e. the current local IMF shifted by $\log_{10}(M_{\mathrm{MIN}}/M_{\mathrm{MIN:\,O}})$, for two different values of M_{MIN}, again chosen so that they deliver $f(8\mathrm{M}_\odot) = 60$ per cent and 90 per cent (equation F3). All five IMFs are normalized so that the total mass of stars is $10^3\,\mathrm{M}_\odot$.

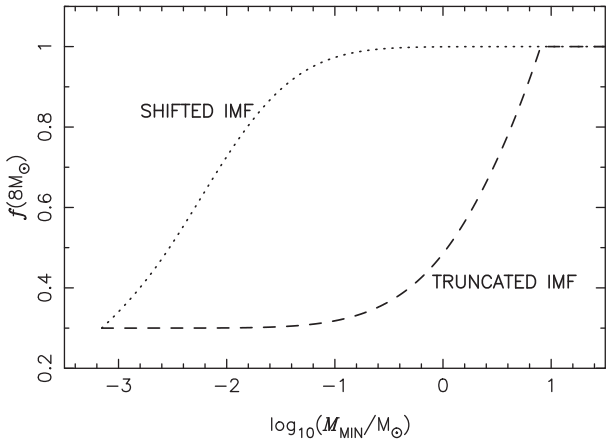

Figure F2. The fraction of mass, $f(8\mathrm{M}_\odot)$, in stars with mass above $8\,\mathrm{M}_\odot$, as a function of M_{MIN}. The dashed curve represents TRUNCATED IMFs, and the dotted curve represents SHIFTED IMFs. See the text for further details.